A quantitative ultrastructural timeline of nuclear autophagy reveals a role for dynamin-like protein 1 at the nuclear envelope

Philip J. Mannino[1], Andrew Perun[1], Ivan V. Surovtsev [1,2], Nicholas R. Ader[1], Lin Shao[1], Elisa C. Rodriguez[1], Thomas J. Melia[1], Megan C. King[1,3], and C. Patrick Lusk[1&]

[1]Department of Cell Biology, Yale School of Medicine, 295 Congress Ave, New Haven, CT, 06520

[2]Department of Physics, Yale University, New Haven, CT, 06511

[3]Department of Molecular Cellular and Developmental Biology, Yale University, New Haven, CT, 06511

[&]Correspondence to C. Patrick Lusk

patrick.lusk@yale.edu

Abstract

Autophagic mechanisms that maintain nuclear envelope homeostasis are bulwarks to aging and disease. By leveraging 4D lattice light sheet microscopy and correlative light and electron tomography, we define a quantitative and ultrastructural timeline of nuclear macroautophagy (nucleophagy) in yeast. Nucleophagy begins with a rapid accumulation of the selective autophagy receptor Atg39 at the nuclear envelope and finishes in ~300 seconds with Atg39-cargo delivery to the vacuole. Although there are several routes to the vacuole, at least one pathway incorporates two consecutive membrane fission steps: inner nuclear membrane (INM) fission to generate an INM-derived vesicle in the perinuclear space and outer nuclear membrane (ONM) fission to liberate a double membraned vesicle to the cytosol. ONM fission occurs independently of phagophore engagement and instead relies surprisingly on dynamin like 1 (Dnm1), which is recruited to sites of Atg39 accumulation by Atg11. Loss of Dnm1 compromises nucleophagic flux by stalling nucleophagy after INM fission. Our findings reveal how nuclear and INM cargo are removed from an intact nucleus without compromising its integrity, achieved in part by a non-canonical role for Dnm1 in nuclear envelope remodeling.

Introduction

The nuclear envelope (NE) establishes the boundary between cytoplasm and nucleoplasm. Although it shares a contiguous lumen with the endoplasmic reticulum (ER), it is functionally specialized by the unique proteomes and lipidomes that distinguish at least three membranes: the inner nuclear membrane (INM) that engages with the genome and in some eukaryotes, a nuclear lamina, an outer nuclear membrane (ONM) that connects with the cytoskeleton, and a pore membrane that houses nuclear pore complexes (NPCs). As for all organelles, NE proteins are subject to proteostasis mechanisms that include the ubiquitin-proteasome and autophagy pathways[1]. These degradative processes are triggered upon molecular damage or genetic perturbation to NE components[2-4], nutrient deprivation[5], mislocalization of integral membrane proteins to the INM[6-8], senescence[9], during the meiotic program[10,11], and in the context of other cellular stresses[12]. Although turnover of the NE is important to maintain cellular homeostasis by combatting the accumulation of deleterious factors associated with disease and aging[13], the underlying mechanisms remain to be fully defined.

Of the two major protein degradation pathways, autophagy recycles a broader spectrum of molecules including protein aggregates, nucleic acids, and lipids[14]. The latter may be particularly important at the nucleus as the NE is sensitive to perturbations in lipid composition[15-18] and metabolism[19-21]. Autophagy delivers molecules (cargo) for degradation in lysosomes (in metazoans) or vacuoles (in yeast and plants) either directly through microautophagy or indirectly through macroautophagy, which incorporates a double membrane autophagosome intermediate[22]. The precursor to the autophagosome, the phagophore or isolation membrane, is a cup-shaped lipid bilayer

61 that forms de novo and expands around cargo with the aid of scaffold proteins like Atg11
62 in yeast or FIP200 in mammals[23]. There are both non-selective and selective
63 macroautophagy pathways with the latter defined by selective autophagy receptors
64 (SARs) that are recruited to specific cargo and interface with the Atg11/FIP200 scaffolds
65 and membrane-associated proteins on the phagophore, most commonly lipidated LC3
66 (Atg8 in yeast)[22].

67 Both micro and macroautophagy pathways act on the nucleus. For example,
68 mammalian cells execute a form of nuclear microautophagy whereby the ONM
69 selectively buds into lysosomes[24]. Similarly, piecemeal microautophagy of the nucleus
70 (PMN) in yeast involves the coordinated evagination of both the INM and ONM directly
71 into the vacuole[25]. The forms of nuclear macroautophagy described to date are
72 comparatively less well understood and atypical as selectivity is imparted by direct
73 interactions between Atg8/LC3 and the cargo instead of through a dedicated SAR.
74 These pathways include the clearance of Lamin B1 under conditions of oncogene-
75 induced senescence[9] and NPCs by "NPC-phagy"[26-28]. In contrast, work in budding yeast
76 identified the first nuclear-specific SAR, Atg39[29], that is required for the degradation of
77 both soluble nuclear and integral membrane cargo[29-31]. However, in this pathway, and
78 indeed all forms of nuclear autophagy, the NE remodeling mechanisms required to
79 selectively remove components of the nucleus, INM, and ONM remain mechanistically
80 opaque.

81 Because Atg39 is a SAR and is consumed by autophagy[29], it provides an ideal
82 molecular handle to investigate the kinetics and NE remodeling steps of a model
83 nuclear macroautophagy (hereafter called nucleophagy) pathway. Atg39 is a single pass

integral ONM protein[32,33] with Atg8 and Atg11 interacting motifs on its cytosolic N-terminus[29]. The C-terminal lumenal domain has several amphipathic helices that engage the lumenal leaflet of the INM[32,33]. Thus, Atg39 forms a translumenal bridge that physically couples the INM and ONM and likely coordinates their remodeling during nucleophagy. Consistent with this, the Atg39 lumenal amphipathic helices are required for nucleophagic degradation of nuclear and INM cargos[32,33]. Further, Atg39 overexpression drives elaborate NE blebbing where both membranes of the NE are evaginated[32,33]. However, as these NE blebs remain associated with the NE in the absence of autophagy induction, there remains uncertainty as to the precise membrane remodeling events orchestrated by Atg39 in the physiological state, which must be understood at the ultrastructural and molecular levels.

Two hypothetical models have been proposed for Atg39-mediated nucleophagy[1]. In the first model, two sequential membrane fission events are invoked, first at the INM to generate an INM-derived vesicle (INMDV) in the perinuclear space/NE lumen and the second at the ONM to release a nucleus-derived vesicle (NDV)(Figure S1A). In the second model, the INM and ONM are simultaneously evaginated and an NDV is liberated from the NE through coincident ONM and INM fission events (Figure S1B). Here, we use a combination of lattice light sheet microscopy (LLSM) and correlative light and electron microscopy (CLEM) and tomography to describe the kinetic and ultrastructural steps of nucleophagy. Our data firmly establish that nucleophagy proceeds through an INMDV intermediate. In at least a third of nucleophagy events, INM fission is followed by an ONM fission step that requires Dnm1, a dynamin-like protein that was formerly established to function only in mitochondrial[34] and

107 peroxisomal[35] fission. Thus, we significantly advance a molecular and morphological
108 understanding of a nucleophagy pathway.

109 **Results**

110 **Dnm1 is required for robust nucleophagic flux**

111 To identify membrane remodeling factors that contribute to nucleophagy, we
112 assessed the autophagic flux of Atg39 by modeling an approach used to monitor ER-
113 phagy[36]. We generated yeast strains producing an Atg39 fusion protein with a variation
114 of the Rosella[37] biosensor that is comprised of a tandem pH-sensitive GFP
115 (pHluorin/pHn) and pH-insensitive mCherry/mCh (Figure 1A, B). Atg39-pHn-mCh was
116 expressed from the *ATG39* chromosomal locus with the endogenous 3'UTR intact. We
117 determined that preserving the *ATG39* 3'UTR was essential for optimal expression of
118 Atg39 fusion proteins, particularly when stimulated under conditions of nitrogen
119 starvation but not Tor1-inhibition using rapamycin (Figure S1C-E).

120 After culturing cells without nitrogen, both red-only and red-green Atg39-pHn-mCh
121 fluorescent foci are observed in wildtype (WT) cells (Figure 1C). We calculated a
122 nucleophagic flux value as a ratio of the number of red fluorescent-only foci (i.e. those
123 delivered to the vacuole where the pHn fluorescence is quenched) to the total number
124 of foci in a cell; this ratio was then normalized to 1 for WT cells. We then evaluated
125 nucleophagic flux values in a candidate collection of yeast strains lacking genes that
126 encode nucleophagy cargos (*TAL1, HEH1*)[29,32,33], contribute to macroautophagy (*ATG8*,
127 *ATG11*)[38,39], PMN (*NVJ1*)[40], NE homeostasis (*HEH1*, *HEH2*, *CHM7*)[41-44], ER-phagy
128 (*VPS13, LST1, SCS2, LNP1*)[45-48], ER shaping/remodeling (*SEY1, RTN1, RTN2,*

Figure 1

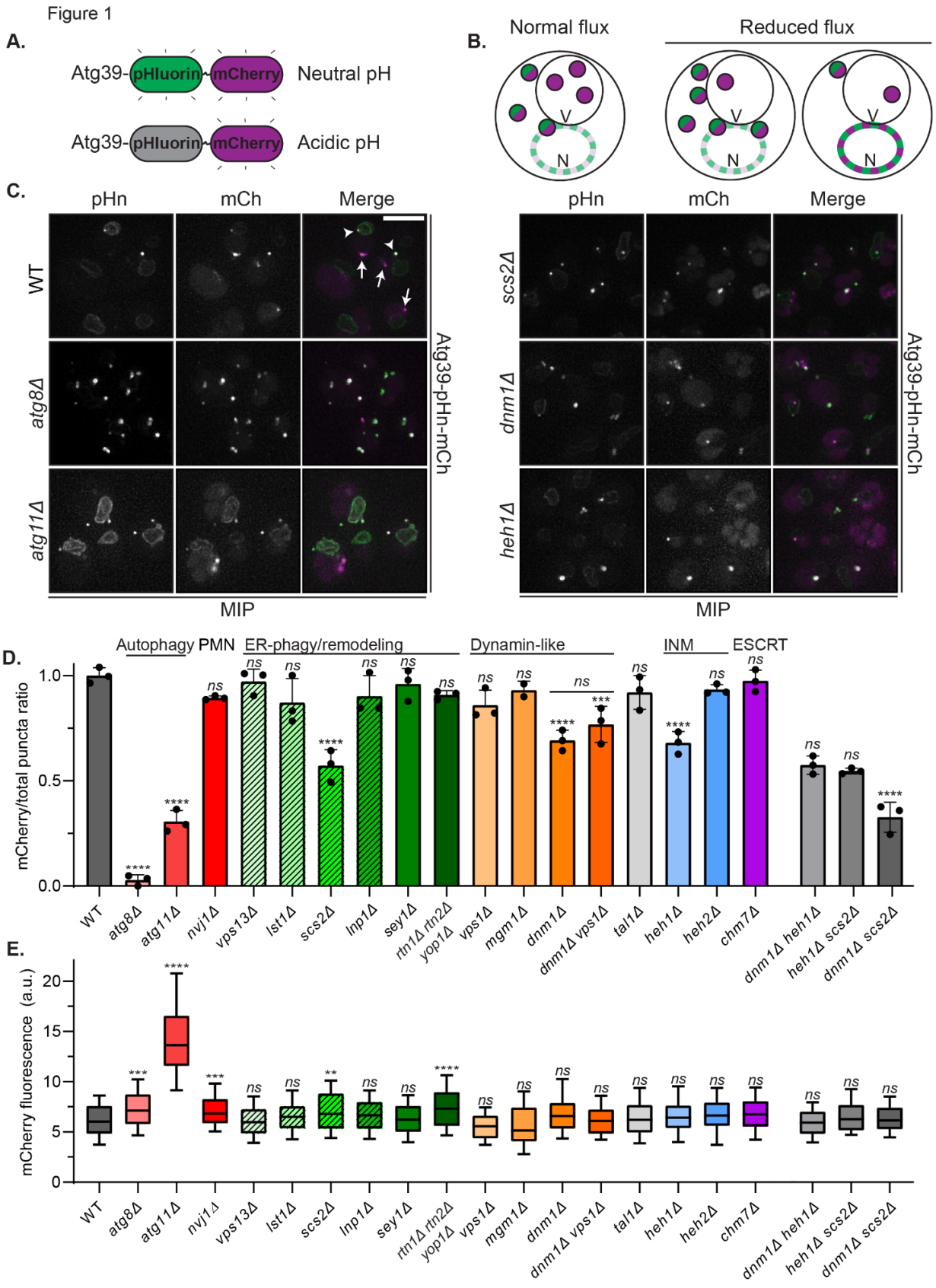
A.
Atg39-pHluorin-mCherry
Neutral pH
Atg39-pHluorin-mCherry
Acidic pH
B.
Normal flux
Reduced flux
V
N
C.
pHn
mCh
Merge
WT
atg8Δ
atg11Δ
scs2Δ
dnm1Δ
heh1Δ
Atg39-pHn-mCh
MIP
D.
Autophagy
PMN
ER-phagy/remodeling
Dynamin-like
INM
ESCRT
mCherry/total puncta ratio
1.0
0.5
0.0
WT
atg8Δ
atg11Δ
nvj1Δ
vps13Δ
lst1Δ
scs2Δ
lnp1Δ
sey1Δ
rtn1Δ rtn2Δ yop1Δ
vps1Δ
mgm1Δ
dnm1Δ
dnm1Δ vps1Δ
tal1Δ
heh1Δ
heh2Δ
chm7Δ
dnm1Δ heh1Δ
heh1Δ scs2Δ
dnm1Δ scs2Δ
E.
mCherry fluorescence (a.u.)
20
15
10
5
0

129

Figure 1 – Dnm1 is required for nucleophagic flux of an Atg39 reporter.

A) Schematic of Atg39-pHn-mCh construct that has red and green fluorescence in neutral pH and only red fluorescence (magenta) in acidic environments like the vacuole.

B) Potential outcomes and interpretation of Atg39-pHn-mCh flux experiment. Schematic of cells (N, nucleus; V, vacuole) with Atg39-pHn-mCh foci diagrammed as either green/magenta or magenta; reduced flux can also manifest as an increase in Atg39-pHn-mCh fluorescence at the NE (far right).

C) Fluorescence micrographs of cells expressing Atg39-pHn-mCh in the indicated genetic backgrounds after 6 h in medium lacking nitrogen. Green (pHn), red (mCh, magenta) channels shown with merge. In all panels a maximum intensity projection (MIP) of a deconvolved z-series of images of entire cell volumes are shown. Arrowheads indicate green/red foci; arrows denote red only foci. Scale bar is 5 µm.

D) Bar graph of the mean ratios of mCherry-only fluorescent Atg39-pHn-mCh foci to the total number of foci in individual cells of indicated genotypes relative to this ratio in WT cells. Genotype labels are organized by established function (described above the graph) of the proteins they are missing. Dashed lines on the green bar graphs indicate genes required for ER-phagy. Error bars are standard deviation from the mean of three biological replicates (dots) except for *mgm1Δ* cells with two. Total n values for each genotype: WT, 279; *atg8Δ*, 240; *atg11Δ,* 414; *nvj1Δ*, 437; *vps13Δ*, 348; *ist1Δ*, 388; *scs2Δ,* 430; *lnp1Δ*, 374; *sey1Δ*, 331; *rtn1Δrtn2Δyop1Δ,* 371; *vps1Δ,* 349; *mgm1Δ*, *205; dnm1Δ,* 372; dnm1*Δ* vps1*Δ,* 355*; tal1Δ 352; heh1Δ*, 486; *heh2Δ*, 357; *chm7Δ*, *501; dnm1Δ heh1Δ, 355; heh1Δ scs2Δ, 339; dnm1Δ scs2Δ, 335.* Ordinary one-way ANOVA with multiple comparisons with ****P<0.0001; ***P<0.001; *ns*, not significant when either compared to the WT value or, for *dnm1Δheh1Δ* and *dnm1Δscs2Δ* to *dnm1Δ*, or, *scs2Δheh1Δ* to *heh1Δ*.

E) Box plot of the mCherry fluorescence intensity (in arbitrary units, a.u.) at the nuclear envelope at regions devoid of Atg39-pHn-mCh foci. Top and bottom of the box are the 75th and 25th percentiles, respectively with median indicated by horizontal bar. Error bars indicate the 10-90th percentiles. Data are from three biological replicates except for the *mgm1Δ* cells where data are from two biological replicates. Total n values for each genotype: WT, 150; *atg8Δ*, 150; *atg11Δ,* 151; *nvj1Δ*, 150; *vps13Δ*, 150; *ist1Δ*, 140; *scs2Δ,* 180; *lnp1Δ,* 150; *sey1Δ,* 150; *rtn1Δrtn2Δyop1Δ* cells, 150; *vps1Δ*, 111; *mgm1Δ*, 115; *dnm1Δ*, 135; *dnm1Δvps1Δ, 150; tal1Δ, 150; heh1Δ*, 151; *heh2Δ*, 128; *chm7Δ*, 150; *dnm1Δheh1Δ,* 150*; heh1Δscs2Δ,* 150*; dnm1Δscs2Δ,* 150. Ordinary one-way ANOVA with multiple comparisons. ****P<0.0001; ***P<0.001; **P<0.01; *ns*, not significant.

YOP1)[49,50], and membrane fission and fusion mechanisms at other organelles (*DNM1, MGM1, VPS1*)[51-53]. Consistent with the conclusion that this approach reported on perturbations to nucleophagy, Atg39-pHn-mCh flux was nearly abolished in *atg8Δ* cells and severely attenuated in the absence of *ATG11* (Figure 1C, D). In the latter case, we also observed an increase of Atg39-pHn-mCh fluorescence throughout the entire nuclear periphery, suggesting that Atg11 may contribute to early nucleophagy events required for Atg39's focal accumulation at the NE (Figure 1C, E).

We did not observe any major impact on Atg39-pHn-mCh flux or NE accumulation after perturbing PMN by deletion of *NVJ1* (Figure 1D, E). Likewise, most tested membrane remodeling deletion strains had normal nucleophagic flux, although we note

140 that there were modest increases in NE fluorescence that met reasonable statistical
141 significance in the context of the *rtn1Δrtn2Δyop1Δ* strain (Figure 1E), which has
142 perturbed ER morphology[50]. In marked contrast, we observed a robust 30-45%
143 reduction in nucleophagy in *scs2Δ*, *dnm1Δ*, and *heh1Δ* strains (Figure 1C, D). Of these,
144 Dnm1 (orthologue of DRP1) stood out as it is part of the dynamin family of GTPases
145 that drive membrane fission[54]. Importantly, although Vps1 acts redundantly with Dnm1
146 in the degradation of peroxisomes[55], deletion of *VPS1* did not further reduce
147 nucleophagic flux of *dnm1Δ* cells (Figure 1D). While it is known that Dnm1 functions at
148 mitochondria and peroxisomes, there is no prior evidence that it acts at the NE.

149 We next tested for epistasis between *DNM1*, *HEH1* and *SCS2* by assessing Atg39-
150 pHn-mCh flux in *dnm1Δheh1Δ*, *dnm1Δscs2Δ,* and *scs2Δheh1Δ* strains. As shown in
151 Figure 1D, only the combined deletion of *DNM1* and *SCS2* led to a synergistic loss of
152 nucleophagic flux that was reduced to levels comparable to those in the *atg11Δ* strain.
153 Curiously, deletion of *SCS2* and/or *DNM1* and even *ATG11* did not appreciably impact
154 the total levels of free pHn ('pHn) generated by vacuolar cleavage of Atg39-pHn-
155 mCherry after 24 h of nitrogen starvation, as assessed by western blot (Figure S1F).
156 Thus, the fluorescence-based assay is more sensitive to measuring nucleophagic flux
157 compared to this end-point assay, but there are clearly even Atg11-independent
158 pathways capable of delivering Atg39 to the vacuole. Two of these pathways are
159 genetically distinguished by deletion of *DNM1* or *SCS2*.

160 **Dnm1 colocalizes with Atg39 during nucleophagy**

161 Because we are most interested in understanding the mechanisms of membrane
162 remodeling at the NE, we focused primarily on the surprising role for Dnm1 in the

163 degradation of Atg39. In a model where Dnm1 functions during nucleophagy, it is
164 expected to engage Atg39. We therefore tested colocalization between endogenously
165 expressed Dnm1-mCherry and Atg39-GFP during LLSM timelapse imaging (10 second
166 intervals) of live cells under nitrogen starvation (Figure 2). To control for spurious
167 colocalization events between the abundant mitochondrial/peroxisomal-localized
168 Dnm1[34] and Atg39 in WT cells, we also performed this analysis in the absence of Fis1
169 (Figure S2), which is required to recruit Dnm1 to mitochondria[51] and peroxisomes[56].
170 Further, as we suspected that any interaction between Dnm1 and Atg39 would be
171 fleeting, we also tested how expression of a dominant-negative *dnm1-K41A* allele[57] that
172 produces a GTPase-dead form of Dnm1 that binds, but does not hydrolyze GTP[57]
173 impacts any colocalization between Dnm1-mCherry and Atg39-GFP (Figure 2; Figure
174 S2).

175 We recorded the timing of colocalization relative to the onset of nucleophagy
176 defined as the first observation of an Atg39-GFP focus in a cell. Using this criterion, we
177 observed colocalization between Atg39-GFP and Dnm1-mCherry in less than 10% of
178 WT and *fis1Δ* Atg39-GFP tracks (Figure 2A, D; S2A). Individual colocalization events
179 persisted for only one frame (i.e. less than 20 seconds; Figure 2E). Interestingly,
180 colocalization between Atg39-GFP and Dnm1-mCherry was much more frequent (25-
181 50% of tracks) when we introduced an untagged copy of *DNM1* into the strains (median
182 time of colocalization of 180 s for WT and 160 s for *fis1Δ,* Figure 2B, D; S2B)
183 suggesting that Dnm1-mCherry may not be fully functional in its ability to bind to the NE
184 during nucleophagy without an unaltered counterpart. Not only was colocalization in this
185 context more frequent, but it often persisted for at least 40 seconds (2-3 frames; Figure

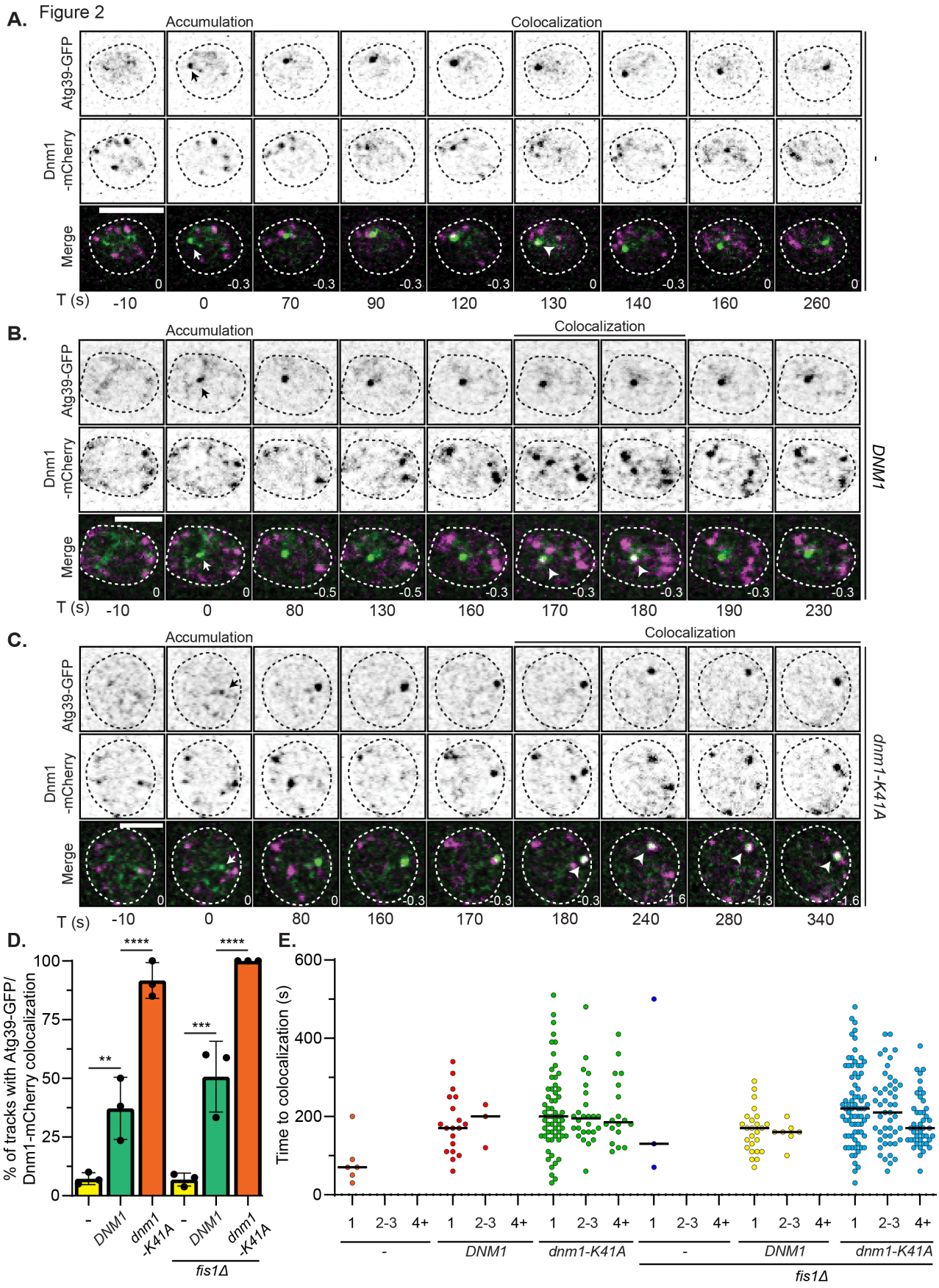
Figure 2
A.
Accumulation
Colocalization
Atg39-GFP
Dnm1 -mCherry
Merge
T (s)
-10
0
70
90
120
130
140
160
260
-
B.
Accumulation
Colocalization
Atg39-GFP
Dnm1 -mCherry
Merge
T (s)
-10
0
80
130
160
170
180
190
230
DNM1
C.
Accumulation
Colocalization
Atg39-GFP
Dnm1 -mCherry
Merge
T (s)
-10
0
80
160
170
180
240
280
340
dnm1-K41A
D.
% of tracks with Atg39-GFP/ Dnm1-mCherry colocalization
100
75
50
25
0
**
****
***
****
-
DNM1
dnm1 -K41A
fis1Δ
E.
Time to colocalization (s)
600
400
200
0
1
2-3
4+
-
DNM1
dnm1-K41A
fis1Δ

186

Figure 2 – Dnm1 is recruited to Atg39 during nucleophagy.

A-C) Inverted fluorescence micrographs of a timelapse series of cells expressing Atg39-GFP and Dnm1-mCherry with and without (-) either an extra copy of *DNM1* or the dominant negative *dnm1-K41A* allele under conditions of nitrogen starvation. Green and red channels shown with merge at indicated times (T) with T=0 s being the first detection of a Atg39-GFP focus (arrow). Arrowheads point to colocalization between Atg39-GFP and Dnm1-mCherry. Numbers in merge are the z-position (in µm) of the image shown in reference to the midplane. Scale bars are 5 µm.

D) Plot of the percentage of Atg39-GFP foci that were continuously tracked from their point of origin by timelapse microscopy that colocalize with Dnm1-mCherry at least once during a given timelapse image series in either WT or *fis1Δ* cells. Data in each column are presented with mean and standard deviation from 3 biological replicates (dots). Columns 1-6 are n=54, 46, 47, 48, 43 and 58 tracks, respectively. Ordinary one-way ANOVA with multiple comparisons. ****P<0.0001; ***P<0.001; **P<0.01.

E) A scatter plot of the time between the appearance of an Atg39-GFP focus and colocalization of Atg39-GFP and Dnm1-mCherry. Data are binned by the number of consecutive frames (10 s intervals) colocalization was observed in WT and *fis1Δ* cells with and without expressing *DNM1* or *dnm1-K41A*. The black bar is the median.

2E) suggestive of a sustained physical interaction. Most strikingly, we observed colocalization between Dnm1-mCherry and Atg39-GFP in virtually all cells in the presence of the *dnm1-K41A* allele. Often the colocalization persisted beyond 40 seconds and sometime lasted throughout entire observation window (>350 seconds; median timing of 190 s for WT and 200 s for *fis1Δ,* Figure 2C, E; S2B). These colocalizations persisted even as the pair of foci moved together (Figure 2C; S2C), strongly suggesting that they associated with the same structure. Thus, taken together, there is a robust engagement of Dnm1 with Atg39 during nucleophagy with virtually all sites of Atg39 accumulation being in principle competent to recruit Dnm1.

Consistent with studies demonstrating that Atg11 directly recruits Dnm1 in the context of mitophagy[58] and pexophagy[55], we also determined that Atg11 was required for the recruitment of Dnm1 to the NE (Figure S3A, B). Further, we detected specific Bimolecular Fluorescence Complementation (BiFC[59], Figure S3C) between Atg11 and Dnm1 tagged with either the N or C-termini of the fluorescent protein Venus suggesting a direct physical interaction between these proteins (Figure S3D). Indeed, BiFC signal

202 was lost upon deletion of the last 30 amino acids of Dnm1 which contains the Atg11
203 binding site[58] (Figure S3D). Importantly, as BiFC between Dnm1 and Atg11 also occurs
204 at mitochondria and peroxisomes undergoing autophagy[55,58], we confirmed that a
205 fraction of the BiFC signal was derived from sites of Atg39 accumulation by
206 colocalization with Atg39-ymTurquoise2 (Figure S3D, E). Thus, Atg11 plays a likely
207 direct role in the recruitment of Dnm1 to Atg39 at the NE.

208 **Quantitative analysis of Atg39 dynamics**

209 To better interpret the timing of Dnm1 recruitment to Atg39, we needed an
210 accounting of the molecular, kinetic, and morphological steps that comprise
211 nucleophagy. We therefore performed LLSM timelapse imaging of Atg39-GFP under
212 conditions of nitrogen starvation in WT cells. To facilitate monitoring the delivery of
213 Atg39-GFP into vacuoles, we performed these experiments in cells expressing Vph1-
214 mCherry to visualize vacuolar membranes. We measured the intensity of Atg39-GFP
215 foci and used commercial (Imaris) and our own particle tracking algorithms[60-62] to
216 quantitatively evaluate their initial appearance at the NE, their rate of growth, and their
217 delivery to the vacuole – all of which occurred at a rate of 1.4 events/cell/hour (Figure
218 S4D; Movie 1).

219 Atg39-GFP was first visible diffusely localized along the nuclear rim before it
220 concentrated into a single focus (Figure 3A). Of note, Atg39 always (*n*=114/114)
221 accumulated directly adjacent to the nucleus-vacuole junction (NVJ), suggesting that
222 nucleophagy may occur at a privileged domain on the NE and/or vacuole (Figure 3A).
223 As with other forms of selective autophagy, we observed that mCherry-Atg8 was
224 recruited near-coincidentally to sites of Atg39-GFP NE accumulation (Figure S4A,B).

Figure 3

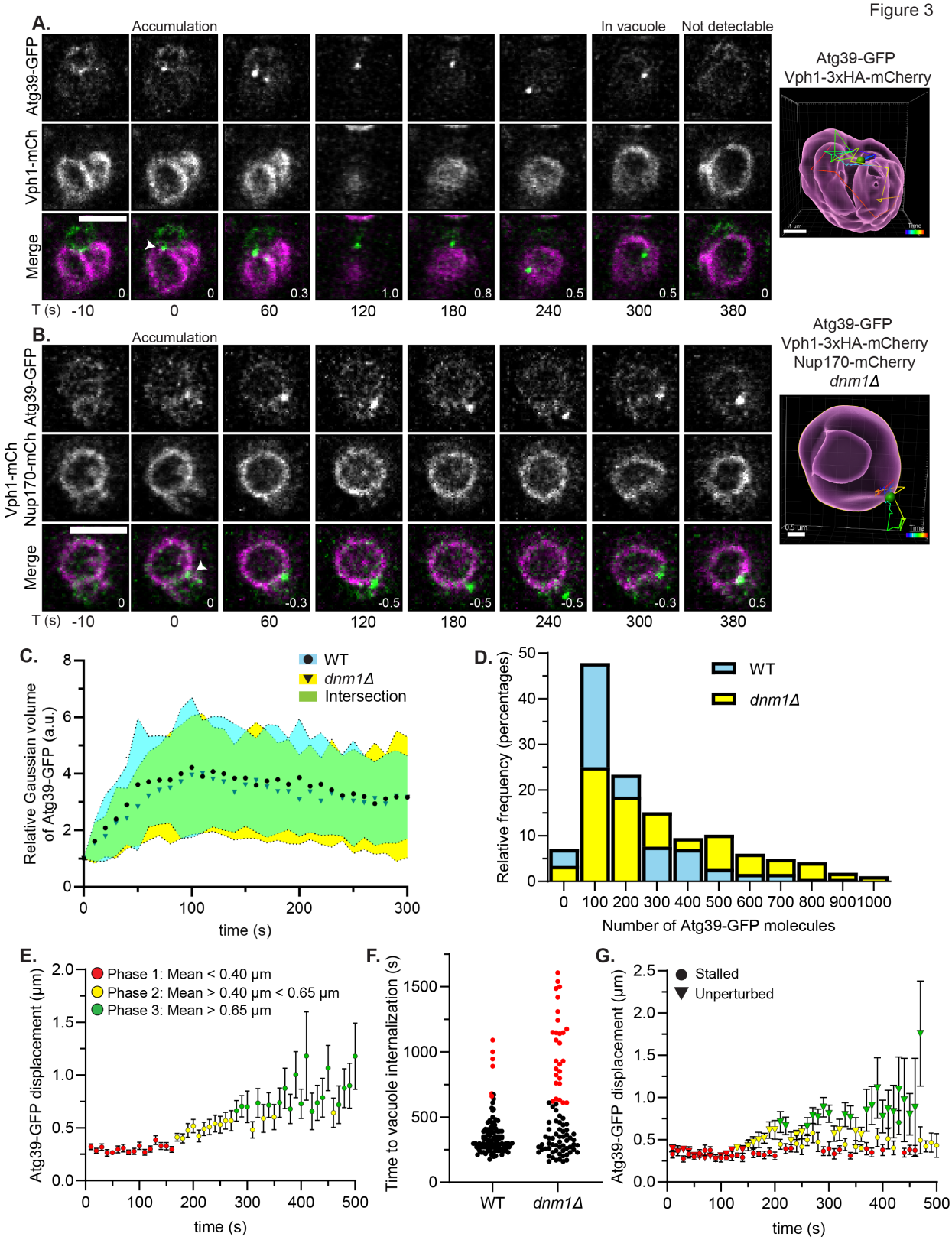
A.
Accumulation
In vacuole
Not detectable
Atg39-GFP
Vph1-mCh
Merge
T (s) -10 0 60 120 180 240 300 380
Atg39-GFP
Vph1-3xHA-mCherry
B.
Accumulation
Atg39-GFP
Vph1-mCh
Nup170-mCh
Merge
T (s) -10 0 60 120 180 240 300 380
Atg39-GFP
Vph1-3xHA-mCherry
Nup170-mCherry
dnm1Δ
C.
WT
dnm1Δ
Intersection
Relative Gaussian volume of Atg39-GFP (a.u.)
time (s)
D.
WT
dnm1Δ
Relative frequency (percentages)
Number of Atg39-GFP molecules
E.
Phase 1: Mean < 0.40 µm
Phase 2: Mean > 0.40 µm < 0.65 µm
Phase 3: Mean > 0.65 µm
Atg39-GFP displacement (µm)
time (s)
F.
Time to vacuole internalization (s)
WT
dnm1Δ
G.
Stalled
Unperturbed
Atg39-GFP displacement (µm)
time (s)

225

Figure 3 – Dnm1 impacts Atg39 dynamics, copy number, and robust delivery to vacuole.

A) Fluorescence micrographs from a timelapse series of WT cells expressing Atg39-GFP and Vph1-mCherry (mCh) in media lacking nitrogen. The images shown are at indicated times (T) with T=0 s being the first detection of a Atg39-GFP focus (arrow), which is followed until Atg39-GFP fluorescence disappears in the vacuole (Quenched). Green and red channels shown with merge. Numbers in merge are the z-position (in µm) of the image shown in reference to the midplane. Scale bar is 3 µm. The panel at right shows a 3D model with particle track of Atg39-GFP focus color coded by time as indicated by key. Vph1-mCherry was rendered as a magenta surface and Atg39-GFP as a green ball. Scale bar length is indicated in the image.

B) As in A but for *dnm1Δ* cells.

C) Atg39-GFP foci intensity versus time after their first detection. Data are normalized to the volume of the Gaussian of the first detection of an Atg39-GFP focus. Circles (WT) and triangles (*dnm1Δ*) indicate the mean and shaded areas are the standard deviation from three biological replicates. For WT cells, *n*=46 tracks, 45 cells. For *dnm1Δ* cells, *n*=44 tracks, 43 cells.

D) Histogram of the distribution (% of total) of the number of Atg39-GFP molecules per focus at steady state in cells of the indicated genotypes cultured for 4 h without nitrogen. A total of 184 and 266 Atg39-GFP foci were analyzed from three biological replicates of WT and *dnm1Δ* cells, respectively.

E) Plot of the mean displacement of Atg39-GFP foci over time in WT cells. Bars are standard error of mean (SEM). The points are colored as indicated in the legend. *n*=40 tracks from 38 cells from three biological replicates.

F) Scatter plot of the time between the initial identification of an Atg39-GFP focus in WT and *dnm1Δ* cells and internalization into the vacuole. Red dots indicate instances in which the Atg39-GFP particle never entered the vacuole after at least ten minutes. For WT cells, *n*=114 tracks, 99 cells, five biological replicates. For *dnm1Δ* cells, *n*=95 tracks, 82 cells, four biological replicates.

G) As in **E** but *dnm1Δ* cells. Atg39-GFP tracks were grouped together based on whether they were internalized (unperturbed) or not (stalled) in vacuoles. The points are colored as indicated in the legend in **E.** *n*=37 unperturbed tracks (triangles), 36 cells and *n*=19 stalled tracks (circles), 19 cells, three biological replicates.

226 Atg39-GFP fluorescence rapidly increased by over 4-fold and then leveled off by ~100
227 seconds before a modest diminishment that likely reflected photobleaching (Figure 3C;
228 blue, circles). A molecular counting strategy based on relating the fluorescence of
229 Atg39-GFP foci to a GFP standard of known copy number (Fta3-GFP[63])(Figure S1G)
230 indicated that the median number of Atg39-GFP molecules in a given focus at steady
231 state was 134 (Figure 3D; blue) with ~50-100 molecules added per minute during the
232 initial phase (Figure 3C,D) likely through the coalescence of smaller Atg39-GFP foci that
233 were detected with faster (2 s/frame) imaging (Figure S4F). Interestingly, robust focal
234 accumulation of Atg39-GFP at the NE was dependent on Atg11: we observed a
235 reduction in the number of Atg39-GFP NE foci/hour in *atg11Δ* cells to ~45% the level of
236 WT or *dnm1Δ* cells (Figure S4C,D). Further, of the Atg39-GFP NE foci that did form,

237 about half had characteristics that were similar to those in WT cells, whereas the other
238 half failed to reach the same apex of fluorescence intensity and ultimately dispersed
239 throughout the NE ("aborted"; Figure S4C,E).

240 To quantitatively describe Atg39's journey from the NE to the vacuole, we
241 measured the displacements of each of 40 Atg39-GFP foci every 10 seconds over 20-
242 minute timelapse experiments from the first frame of their NE focal accumulation. A
243 consistent theme emerged in which the Atg39-GFP tracks could be empirically
244 categorized into three bins based on characteristic mean displacements for each time
245 point (Figure 3E). In an initial phase that extended until ~160 seconds, Atg39-GFP foci
246 were constrained with average displacements of 0.30 ± 0.03 μm (Figure 3E; red). This
247 was followed by ~100 seconds where the average displacement roughly doubled to
248 0.52 ± 0.08 μm (Figure 3E; yellow). Finally, at ~280 seconds Atg39-GFP foci entered a
249 highly mobile state with a mean displacement of 0.82 ± 0.18 μm (Figure 3E; green).
250 Thus, Atg39-GFP foci transition from a constrained to a highly mobile state during
251 nucleophagy.

252 The categorization of Atg39-GFP dynamics into three states provided a useful
253 framework to interpret and temporally align key molecular events. For example, manual
254 inspection of all Atg39-GFP tracks with the vacuole membrane marker (Vph1-mCherry)
255 indicated that delivery into the vacuole lumen occurred within a range of 3 to 8 minutes
256 after Atg39-GFP accumulation with a median of ~284 seconds (Figure 3A, F), notably
257 like the timing of the transition from phase 2 to 3. Likewise, the transition from phase 1
258 to 2 occurs with timing that corresponds to the median timing of Dnm1 recruitment
259 (~170 seconds after Atg39-GFP accumulation, Figure 2E). Further, and consistent with

260 the interpretation that phase 1 reflects the dynamics of Atg39 at the NE, we observed
261 that a model INM cargo (Figure S5A) colocalizes with Atg39-GFP foci with a mean
262 timing of ~80 seconds after Atg39-GFP accumulation (Figure S5B, C). Thus, together
263 these data predict that Dnm1 contributes to a key transition step in nucleophagy that
264 corresponds to a step after cargo delivery and between the NE and vacuole.

265 **Nucleophagy stalls in the absence of Dnm1**

266 To explore a model in which Dnm1 acts during nucleophagy, we monitored
267 Atg39-GFP dynamics in *dnm1Δ* cells. Interestingly, early events including the formation
268 of the Atg39-GFP foci proximal to the NVJ (Figure 3B) and the initial rate of Atg39-GFP
269 accumulation (Figure 3C; yellow, triangles) were indistinguishable between WT and
270 *dnm1Δ* cells. However, analyzing Atg39-GFP copy number within individual foci at
271 steady state revealed an increase to a median of 264 molecules in *dnm1Δ* cells
272 compared to 134 in WT cells (Figure 3D; yellow). Taken together, these data suggest
273 that *dnm1Δ* cells contain a population of Atg39-GFP foci that accumulate additional
274 molecules in a timeframe beyond 300 seconds, implying their delivery to the vacuole
275 may be impaired.

276 Our prior observations suggested only a partial compromise in nucleophagic flux
277 in the absence of *DNM1* (Figure 1D), and indeed, in the instances where Atg39-GFP
278 was delivered to the vacuole in *dnm1Δ* cells, it did so with timing comparable to WT
279 cells (Figure 3F; black dots). However, 33% of Atg39-GFP foci that were tracked from
280 their NE accumulation forward failed to enter the vacuole over the experimental
281 timeframe compared to only 6% in WT cells (Figure 3F; red dots, Figure S5D). Thus,
282 consistent with the nucleophagic flux assay, these observations suggest that Dnm1 is

283 required for the delivery of at least a third of Atg39 to the vacuole. We next assessed
284 the dynamics of Atg39-GFP foci in *dnm1Δ* cells. As our data suggested at least two
285 fates of Atg39 in *dnm1Δ* cells, we measured the displacement of the "stalled" (Dnm1-
286 dependent; Figure 3G; circles) and "unperturbed" (Dnm1-independent; Figure 3G;
287 triangles) Atg39-GFP tracks separately and color-coded the data to reflect the three
288 states defined in Figure 3E. Strikingly, whereas the unperturbed tracks exhibited
289 dynamics that were similar to WT cells, the stalled tracks had mean displacements that
290 mirror those in the first phase, consistent with the notion that the transition from phase 1
291 to phase 2 was disrupted by loss of *DNM1* in these cells (Figure 3G; circles). Indeed,
292 the relative time that the stalled Atg39 tracks spent in phase 1 doubled compared to
293 both WT cells and the unperturbed tracks in *dnm1Δ* cells (Figure S5E). Thus, these
294 data support a model in which Dnm1 is required to release Atg39 from the confines of
295 the NE in at least a third of all nucleophagy events.

296 **Nucleophagy proceeds through a lumenal vesicle intermediate**

297 We next sought to correlate Atg39's dynamics in WT and *dnm1Δ* cells to an
298 ultrastructural description of nucleophagy by CLEM and tomography. This analysis was
299 enabled by the recently developed hyper folder YFP (hfYFP), which retains more
300 fluorescence compared to mEGFP following fixation, staining, and embedding[64]. We co-
301 expressed Nup170-mCherry and Vph1-mCherry to provide additional landmarks to
302 determine the position of Atg39-hfYFP relative to the nucleus and vacuole, respectively.
303 As we lack an approach to synchronize nucleophagy, we acquired tomograms from
304 randomly selected Atg39-hfYFP foci, avoiding those that were within the vacuole lumen.
305 As CLEM is laborious and low-throughput, we used probability theory to establish a

Figure 4

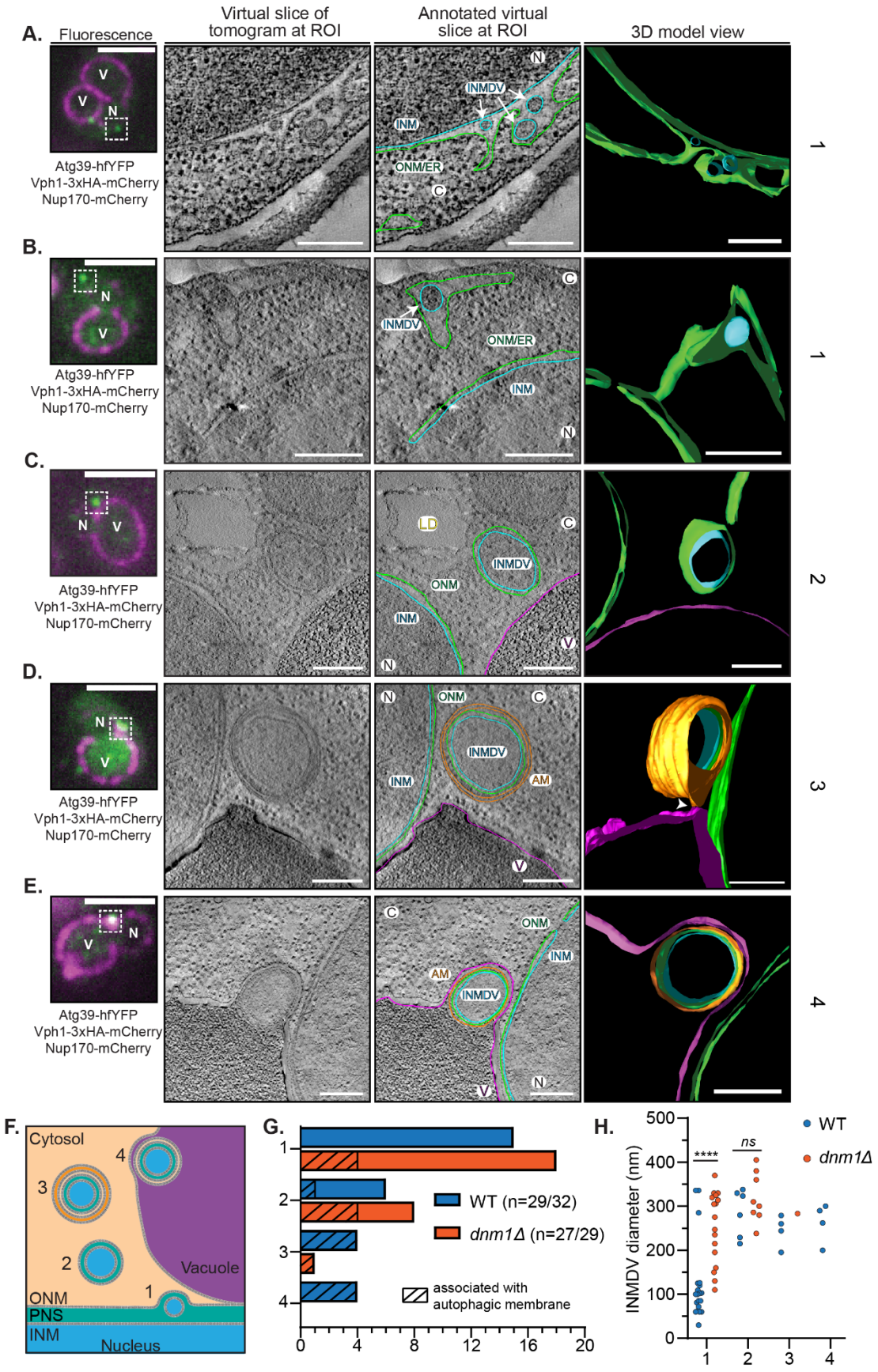
A.
Fluorescence
Virtual slice of tomogram at ROI
Annotated virtual slice at ROI
3D model view
V
V
N
INMDV
INM
ONM/ER
C
N
1
Atg39-hfYFP
Vph1-3xHA-mCherry
Nup170-mCherry
B.
N
V
INMDV
ONM/ER
INM
C
N
1
Atg39-hfYFP
Vph1-3xHA-mCherry
Nup170-mCherry
C.
N
V
LD
C
INMDV
ONM
INM
V
N
2
Atg39-hfYFP
Vph1-3xHA-mCherry
Nup170-mCherry
D.
N
V
N
ONM
C
INMDV
INM
AM
V
3
Atg39-hfYFP
Vph1-3xHA-mCherry
Nup170-mCherry
E.
V
N
C
ONM
INM
AM
INMDV
V
N
4
Atg39-hfYFP
Vph1-3xHA-mCherry
Nup170-mCherry
F.
Cytosol
4
3
2
1
Vacuole
ONM
PNS
INM
Nucleus
G.
1
2
3
4
WT (n=29/32)
dnm1Δ (n=27/29)
associated with autophagic membrane
0
4
8
12
16
20
H.
500
400
300
200
100
0
INMDV diameter (nm)
****
ns
WT
dnm1Δ
1
2
3
4

306

Figure 4 – Nucleophagy proceeds through a lumenal vesicle intermediate.

A-E) CLEM/tomography of sites of Atg39-hfYFP foci. From left to right: fluorescence image of WT cells expressing Atg39-hfYFP (green), Vph1-mCherry and Nup170-mCherry (magenta). Scale bar is 3 µm. EM tomogram acquired of boxed region in fluorescence image and tomogram virtual slice without and with annotation shown alongside a snapshot of a 3D model. Arrows point to INMDVs. ONM is green, INM is light blue, phagophore/autophagosome is orange, vacuole membrane is magenta. Scale bar is 200 nm. C, cytosol; N, nucleus; V, vacuole; ONM, outer nuclear membrane; INM, inner nuclear membrane; ER, endoplasmic reticulum; INMDV, inner nuclear membrane derived vesicle; AM, autophagic membrane; LD, lipid droplet. Numbers at right refer to classification scheme in **F**. Arrowhead indicates a site of close apposition between the outer membrane of the autophagosome and the vacuole in **D**.

F) Schematic representation of the morphologies observed at Atg39-hfYFP foci, which are classified by number to facilitate quantification.

G) Bar graph of the number of tomograms with observed morphology categories (**F**) in WT and *dnm1Δ* cells. Dashed lines indicate the observation of phagophore membranes. Tomograms were acquired at 32 Atg39-hfYFP foci and 29 Atg39-hfYFP foci from multiple thick sections of a WT and *dnm1Δ* embedded sample, respectively.

H) Scatter plot of INMDV diameters in each morphological category described in **F** in WT and *dnm1Δ* cells. For category 1, n=20 vesicles in WT and n=17 vesicles in *dnm1Δ* cells. For category 2, n=6 vesicles for WT and n=8 vesicles for *dnm1Δ* cells. For category 3 n=4 vesicles for WT and n=1 vesicle for *dnm1Δ* cells. For category 4 n=4 vesicles for WT and n=0 vesicles for *dnm1Δ* cells. Unpaired two-sided t tests, ****P<0.0001; *ns*, not significant.

target of ~30 tomograms, which would allow us to capture at least one image representative of all morphological steps that last longer than 30 seconds given that it takes ~300 seconds to complete nucleophagy (see methods). Thus, morphologies comprising phase 1 (~160 seconds) and 2 (~100 seconds) should be highly represented and perhaps those invisible to the quantitative light microscopy analysis could also be revealed.

We obtained 32 tomograms in WT cells where we correlated the fluorescence of Atg39-hfYFP to the underlying ultrastructure (Figure 4A-E; Figure S6A-E). We observed several morphologies that are schematized with categorization labels (1-4) in Figure 4F; the number of tomograms representative of each category is plotted in Figure 4G (blue bars). We made several observations: 1) Approximately half (15/32) of the Atg39-hfYFP foci correlated to regions of NE (Figure 4A) or, surprisingly, ER (Figure 4B; Figure S6A-C), with intralumenal vesicles that we interpret as INMDVs; in the latter we often visualized a nearby ER-NE junction within the 3D volume of the tomogram (e.g. Figure

321 4B, see 3D model) while some appeared in the cortical ER proximal to the plasma
322 membrane (Figure S6C). The observation of INMDVs confirmed that INM fission occurs
323 prior to ONM fission (Model 1; Figure S1A). Of additional interest, INMDVs at the NE
324 were associated with an expansion of the ONM (Figure 4A) suggesting that these
325 events may occur alongside membrane biosynthesis and/or recruitment mechanisms. 2)
326 There were no structures that resembled a phagophore near any Atg39-hfYFP focus
327 that correlated to INMDVs in the NE or ER (Category 1). Moreover, although 6
328 tomograms contained apparent NDVs that had been presumably liberated from the
329 NE/ER (Category 2; Figure 4C), only one of these revealed what appeared to be a
330 phagophore in the process of engulfing the structure (Figure S6D). We did, however,
331 observe 4 Atg39-hfYFP foci that correlated to a vesicle enclosed by 4 membranes,
332 which we interpret to be an NDV within an autophagosome (Category 3; Figure 4D). 3)
333 Atg39-hfYFP foci that were observed to be proximal to the vacuole by fluorescence
334 demarked several interesting morphologies that suggest different fates for the
335 autophagosome containing an NDV. For example, we observed close apposition/contact
336 sites between the vacuole and autophagosome (Figure 4D; arrowhead, Movie 2), which
337 was evocative of a kiss and run-type mechanism that might deliver vacuolar degradative
338 enzymes in addition to the more expected direct vacuole fusion (Category 4; Figure 4E).
339 We also observed Atg39-hfYFP foci that overlapped with Vph1-mCherry signal that
340 correlated with a vesicle containing membrane fragments that we presume to be
341 derived from an NDV and autophagosome (Figure S6E). 4) Lastly, we noted that the
342 diameters of the INMDVs were 25-125 nm when found within the NE/ER lumen (with a
343 few exceptions) but were 200-350 nm within NDVs in the cytosol (Figure 4H; blue dots).

344 Making the reasonable assumption that the NDVs arose from the INMDVs in the NE/ER
345 lumen, the implication is that the INMDVs may fuse together before they are released
346 as NDVs into the cytosol. Indeed, we occasionally observed multiple closely apposed
347 INMDVs in the NE/ER lumen that correlated with a single Atg39-hfYFP focus (Figure
348 4A, Figure S6A) including one example in which we captured two vesicles connected by
349 a narrow membrane neck as if undergoing fusion or fission (Figure S6B), further
350 supporting this idea. If smaller INMDVs fuse before they are liberated within a cytosolic
351 NDV, a prediction would be that larger vesicles would accumulate in the NE/ER lumen
352 upon inhibition of ONM/ER scission.

353 **Dnm1 is required for ONM scission**

354 To better understand how Dnm1 contributes to nucleophagy, we next performed
355 CLEM to localize 29 randomly selected non-vacuolar Atg39-hfYFP foci in the context of
356 the ultrastructure in *dnm1Δ* cells. We categorized the observed morphologies as in WT
357 cells (Figure 4F). Consistent with the idea that nucleophagy is stalled in the absence of
358 *DNM1*, we did not observe any examples of autophagosome-vacuole fusion (Category
359 4; Figure 4G; red). Instead, there was an increase in the labeling of structures that
360 comprise early events like those containing INMDVs within the NE/ER lumen (Category
361 1; Figure 4G, Figure 5A, B, Figure S7A, B). Note that this class also incorporates
362 INMDVs found within the cortical ER suggesting that a pathway for INMDVs to travel
363 throughout the ER lumen is retained in the *dnm1Δ* cells (Figure S7E). Most strikingly,
364 unlike in WT cells where we did not observe engagement of phagophores with Atg39-
365 hfYFP positive morphologies that labeled INMDVs in the NE/ER, a quarter of category 1
366 tomograms had membranes that appeared as ribbons in the 3D segmentation of the

Figure 5

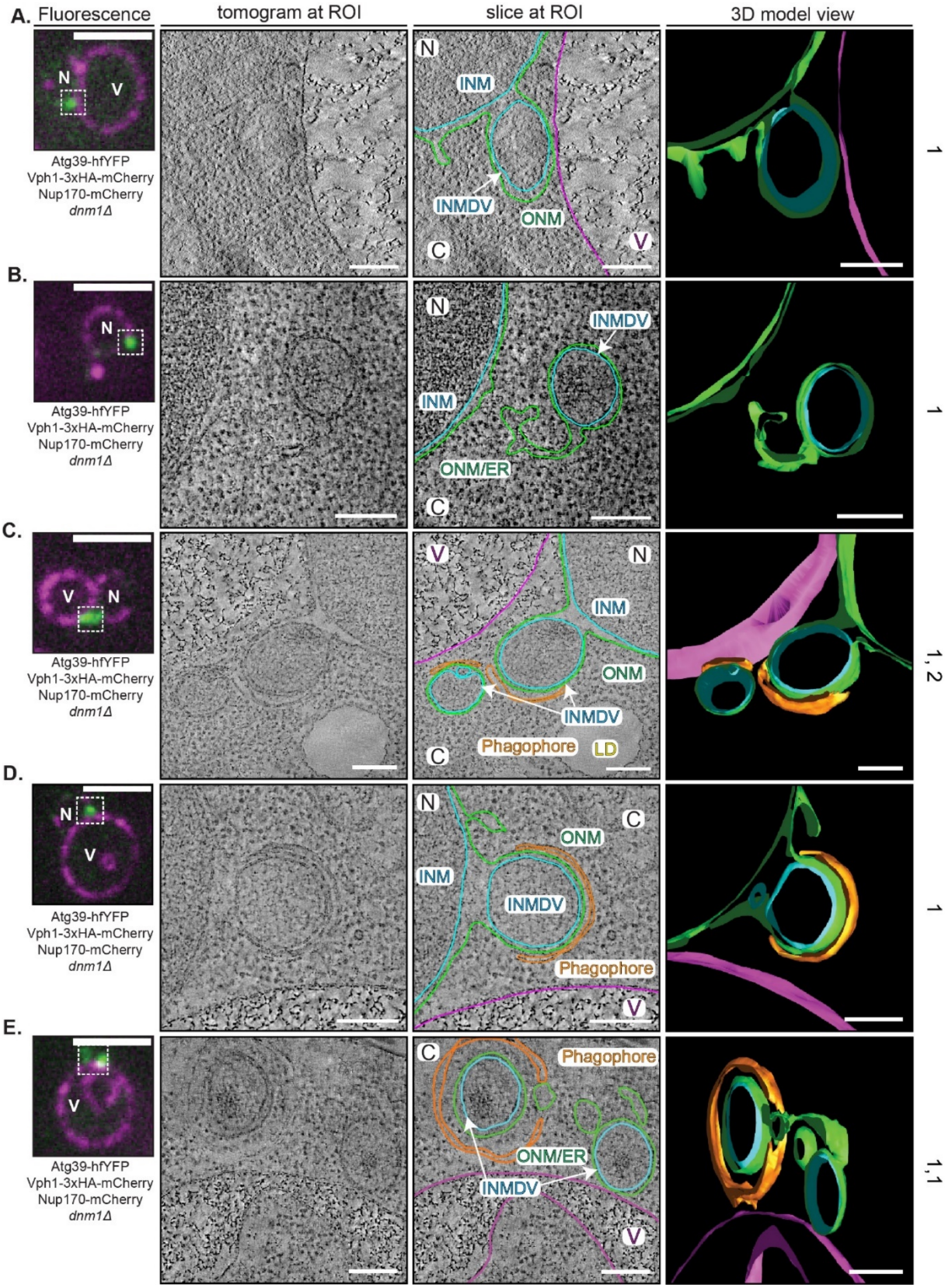
A. Fluorescence
Virtual slice of tomogram at ROI
Annotated virtual slice at ROI
3D model view
N
V
INM
INMDV
ONM
C
Atg39-hfYFP
Vph1-3xHA-mCherry
Nup170-mCherry
dnm1Δ
1
B.
ONM/ER
1
C.
Phagophore
LD
1, 2
D.
1
E.
1,1

367

Figure 5 – Dnm1 is required for ONM fission.

A-E) CLEM/tomography of sites of Atg39-hfYFP foci in *dnm1Δ* cells. From left to right: fluorescence image of *dnm1Δ* cells expressing Atg39-hfYFP (green), Vph1-mCherry and Nup170-mCherry (magenta). Scale bar is 3 µm. EM tomogram acquired of boxed region in fluorescence image and tomogram virtual slice without and with annotation shown alongside a snapshot of a 3D model. Arrows point to INMDVs. ONM/ER is green, INM is light blue, phagophore/autophagosome is orange, vacuole membrane is magenta. Scale bar is 200 nm. C, cytosol; N, nucleus; V, vacuole; ONM, outer nuclear membrane; INM, inner nuclear membrane; ER, endoplasmic reticulum; INMDV, inner nuclear membrane derived vesicle; AM, autophagic membrane. Numbers at right refer to classification scheme in Figure 4F.

368 whole tomogram volume that were in close apposition to and followed the contour of the
369 ONM (Figure 5C-E, Figure S7C, Movie 3). In several examples as in Figure 5D and 5E,
370 the phagophores surrounded (but failed to fully encompass) the NE-derived
371 membranes. Indeed, the phagophore rim appeared obstructed by NE which would need
372 to be cleared by a membrane fission mechanism for phagophore closure to occur.
373 Consistent with this interpretation, we only observed a single Atg39-hfYFP focus within
374 a fully sealed autophagosome in this dataset (Figure 4G). Interestingly, we also
375 observed a four-fold increase in structures we identified as NDVs surrounded by
376 phagophores in *dnm1Δ* cells compared to WT cells (Figure 4G, Figure S7D), although it
377 is likely that at least some of these structures are category 1 but are miscategorized
378 because their NE/ER connections are outside of the tomogram volumes.

379 Additional evidence for stalling of nucleophagy at a step where membrane fission
380 mechanisms must be invoked is also apparent in the sizes of the INMDVs in *dnm1Δ*
381 cells. Indeed, although in WT cells INMDVs within the NE/ER lumen tended to be 25-
382 125 nm in diameter (Category 1; Figure 4H), they were significantly larger (from 100-
383 400 nm; Figure 4H; red dots) in *dnm1Δ* cells and resembled those that were found only
384 in WT cell NDVs, i.e. after they had been released from the NE/ER. These data thus
385 suggest that a delay in an ONM fission mechanism would allow the buildup of additional
386 membrane and perhaps cargo in the INMDV. Such an idea is also supported by the

387 observation that there is a higher copy number of Atg39-GFP within individual foci in
388 *dnm1Δ* cells (Figure 3D). Thus, we conclude that Dnm1 executes ONM fission.
389

390 **Discussion**

391 We have determined the kinetic, molecular, and morphological events that
392 comprise selective Atg39-mediated nucleophagy in budding yeast that is summarized in
393 Figure S8. At the level of the light microscope, nucleophagy begins with rapid (~50-100
394 molecules/min) local accumulation of Atg39 at a site adjacent to the NVJ, which likely
395 occurs concomitantly with cargo capture, and is followed by its delivery to the vacuole in
396 approximately 5 minutes (Figure 3F). We estimate, based on the surface area of INM
397 that is captured in the INMDVs and the rate of nucleophagy (1.4/cell/hour; Figure S4D),
398 that ~80% of the INM is recycled over a 24-hour period when cells are starved of
399 nitrogen. Thus, nucleophagy may help rejuvenate the INM.

400 The data support that there are at least two parallel nucleophagy pathways
401 responsible for the ultimate delivery of Atg39 to the vacuole, one of which is dependent
402 on Dnm1 and the other on Scs2 and likely other yet to be defined factors. As virtually all
403 CLEM micrographs of Atg39 foci revealed the presence of intralumenal vesicles that we
404 interpret to be INMDVs, we suggest that while both pathways incorporate an INM fission
405 mechanism that likely requires the lumenal amphipathic helices of Atg39[32], the Dnm1-
406 dependent nucleophagy pathway requires a second membrane fission reaction
407 executed at the ONM that liberates an NDV to the cytosol. Our data strongly implicate
408 Dnm1 as a key player in ONM fission. This conclusion is supported by several data
409 including the robust association of Dnm1 with Atg39-containing structures (Figure 2)

410 and the buildup of likely stalled nucleophagy intermediates at the NE in *dnm1Δ* cells
411 (Figure 3; 5). Interestingly, the data also support that a C-terminal fusion of Dnm1
412 cannot fully engage the ONM as it does at other organelles like mitochondria[65]. Indeed,
413 we only observe robust association of Dnm1-mCherry with Atg39-GFP in the presence
414 of endogenous Dnm1 or the GTP-locked dominant negative. We speculate that there
415 may be ONM-specific constraints that preclude engagement by the Dnm1-mCherry
416 fusion - perhaps an inability to form a polymer that can encircle an ONM neck. Although
417 the nature of such constraints remains to be discovered, they hint that the ultimate
418 mechanism of ONM fission driven by Dnm1 may have unique characteristics at the NE
419 that await discovery.

420 Despite the potential for a unique Dnm1-mediated fission mechanism at the NE,
421 the data support that the mechanism of Dnm1 recruitment to Atg39 is analogous to how
422 Dnm1 is recruited to sites of Atg32-mediated mitophagy and requires a biochemical
423 interaction between Dnm1 and Atg11[58]. This conclusion is supported by the requirement
424 of Atg11 for Dnm1 recruitment to the NE and the observation of specific BiFC between
425 Atg11 and Dnm1 (that colocalizes with Atg39) and that depends on an Atg11-interacting
426 motif in Dnm1 (Figure S3C, D). How this interaction is ultimately regulated to catalyze
427 ONM fission is not known but may rely on the coordination between Atg11's two
428 apparent roles during nucleophagy. Specifically, in addition to recruiting Dnm1, Atg11
429 contributes to clustering of Atg39 (Figure S4C) to help enforce that Atg39 copy number
430 reaches a critical threshold before it is liberated from the NE, which we suggest is
431 around 150 molecules (Figure 3 C, D). As the copy number is stable after it is released
432 from the nucleus (until its vacuolar degradation), we surmise that Atg11 recruits Dnm1

433 once this critical threshold copy number of Atg39 is reached. In an alternative but non-
434 mutually exclusive model, if we impose a correlation between Atg39 copy number and
435 INMDV size (with the consideration that INMDVs within the NE/ER lumen are typically
436 small, from 50-100 nm with only a handful at 300 nm (Figure 4H)), a reasonable
437 conclusion is that Dnm1 acts once the INMDVs reach ~200-300 nm in diameter, well
438 within the experimentally-determined size of cytosolic NDVs (median of 300 nm). Such
439 a conclusion is also supported by the observation that we only detect larger diameter
440 INMDVs stuck at the NE when ONM fission is inhibited (Figure 4H). Thus, future studies
441 will be needed to explore the relationship between Atg39 copy number and/or INMDV
442 size and how these factors influence the Atg11-dependent recruitment of Dnm1 for
443 ONM scission.

444 That ONM scission may only occur once an INMDV reaches a certain size raises
445 the question of the mechanism of INMDV growth. Indeed, as there appears to be a
446 progression from 50-100 nm to much larger 200-400 nm diameter vesicles in the NE/ER
447 lumen, we must entertain the possibility that these vesicles enlarge by INMDV fusion
448 with the caveat that we cannot fully rule out that we failed to ascertain the fate of the
449 smaller vesicles. Although direct evidence for INMDV fusion is scant, one could interpret
450 the quanta-like merging of Atg39-GFP foci during Atg39 growth within such a framework
451 (Figure S4F). Further, we observed one example of two INMDVs fusing (Figure S6B).
452 As we expect INMDV fusion to be a short-lived event, even capturing this single
453 snapshot speaks to its potential prevalence. How INMDV fusion is achieved is a
454 mystery but would almost certainly require a protein fusogen on the lumenal face of the
455 vesicle membrane. Should such a fusogen exist, one must then consider that INMDVs

456 could also fuse back to the INM or with the ONM or ER membranes. This idea is
457 particularly interesting in the context of so-called NE budding/egress pathways where
458 nuclear cargo (e.g. viruses[66] or large ribonucleoproteins[67]) are packaged into lumenal
459 vesicles that then fuse with the ONM to allow for their cytosolic delivery. Whether there
460 is a functional relationship between NE budding and nucleophagy will require further
461 study and better molecular markers of the NE budding process in other model systems.

462 To continue the analogy with NE budding, we also made the surprising
463 observation of INMDVs within the cortical ER in both WT (Figure S6C) and *dnm1Δ*
464 (Figure S7E) cells. As we only observe a stalling of one third of nucleophagy events in
465 *dnm1Δ* and the associated Atg39-GFP foci appear stuck at the NE, we propose that
466 INMDVs that escape the ONM and enter the broader ER lumen cannot be targeted by
467 Dnm1 and must therefore be degraded by other ER-phagy type pathways that would be
468 predicted to depend on Scs2 (Figure S8A) or other Atg11-independent mechanisms that
469 await discovery (Figure 1; Figure S1F). Consistent with a role for Scs2, it has been
470 implicated in ER-phagy of the cortical ER at sites of endocytosis[48]. It will be exciting to
471 understand whether there is a functional decision made by cells to engage the Dnm1 or
472 Scs2-dependent pathways, but it is worth noting that we often observe INDMVs being
473 generated into the lumen of junctions between the ER and NE (Figure 4A)[32]. Thus, it is
474 possible that under these circumstances there is a direct delivery of some INMDVs into
475 the ER lumen that allows them to escape Dnm1-targeting.

476 That there may be at least two pathways that allow INMDVs to exit the NE, one
477 through Dnm1 and one through NE-ER junctions into the cortical ER, suggests
478 additional mechanistic differences between nucleophagy and other organelle selective

479 autophagy pathways. Indeed, most selective autophagy pathways are thought to occur
480 through a tight coupling of cargo capture by SARS with Atg8-coupled phagophore
481 membranes that is coordinated by scaffold proteins like Atg11[23]. Curiously, however,
482 even though we do observe the near simultaneous recruitment of Atg8 at the point of
483 Atg39 local accumulation at the NE by light microscopy (Figure S4A, B), we failed to
484 detect any obvious membranes that resemble growing phagophores at the NE of WT
485 cells by CLEM. There are several plausible explanations for these potentially
486 contradictory results. First, the small vesicles that may make up nascent phagophores
487 may simply be undetectable in the EM. We do not favor this interpretation as our EM is
488 of high quality with excellent preservation and staining of membranes. Second, Atg8
489 could be directly conjugated to the ONM (or to proximal vacuole membranes)
490 reminiscent of the proposed conjugation of LC3 to the INM during the autophagic
491 degradation of Lamin B1[9]. Finally, non-lipidated Atg8 could associate with Atg39 or with
492 the preautophagosomal structure, the site of autophagosome assembly, perhaps in a
493 poised state[68] ready to be rapidly conjugated onto a nascent phagophore after the
494 release of an NDV by Dnm1. In sum, our study provides a compelling explanation for
495 how nuclear and INM cargo can be delivered to vacuoles while maintaining nuclear
496 envelope integrity through an unexpected ONM fission mechanism mediated by Dnm1.

Acknowledgments

We thank the Center for Cellular and Molecular Imaging for assistance with electron microscopy, particularly M. Graham, Z. Zuo, and X. Liu. We are grateful to C. Kraft, M. Graef and L. Lackner for yeast strains. Thank you to K. Li for technical support. This work was funded by the following grants from National Institutes of Health (NIH): R56AG071201 and R21 AG058033 to C.P.L. and T.J.M.; R01 GM105672 to CPL; F32 GM139285 to N.R.A.; F31 AG069490 to P.J.M.

Author Contributions

Conceptualization: P.J.M., C.P.L.; Methodology: P.J.M, A.P., I.S., N.R.A., L.S., E.R.; Investigation: P.J.M., A.P., I.S., N.R.A.; Validation: P.J.M., A.P.; Data curation: P.J.M., A.P., I.S., N.R.A.; Formal Analysis: P.J.M., A.P., I.S., N.R.A.; Funding acquisition: P.J.M., T.J.M., C.P.L.; Visualization: P.J.M., A.P.; Project administration: P.J.M., M.C.K., C.P.L.; Resources: L.S., C.P.L.; Software: A.P., I.S., L.S.; Supervision: T.J.M., M.C.K., C.P.L.; Writing – original draft: P.J.M., C.P.L.; Writing – review and editing: All authors

Competing interests

The authors have no competing interests to declare.

514 **Materials and Methods**

515 ***Yeast culturing conditions and autophagy induction***

516 All experiments were performed at 30°C. Budding yeast (*S. cerevisiae*) were
517 cultured in YPA (1% Bacto-yeast extract (Y), 2% Bacto-peptone (P), 0.025% adenine
518 hemi-sulfate (A; Sigma)) supplemented with 2% glucose (D; Sigma) or in csm (complete
519 supplement mixture; Sunrise Science Products) to maintain selection for centromeric
520 plasmids. For one experiment, we used S. pombe strain MKSP3186, which was
521 cultured overnight in YE5S (yeast extract (YE), 250 mg/L adenine, histidine, leucine,
522 uracil, and lysine hydrochloride).

523 To induce autophagy by nitrogen starvation, cells in log phase were washed and
524 resuspended in synthetic defined medium lacking nitrogen (sd-N) (0.17% Difco Yeast
525 Nitrogen Base without amino acids and ammonium sulfate, and 2% D). Samples were
526 collected at time points indicated in the figures and were prepared for extraction of RNA,
527 fluorescence microscopy, or immunoblotting as described below.

528 To induce autophagy by inhibiting Tor1 kinase by treatment with rapamycin,
529 rapamycin (in DMSO; Sigma-Aldrich) was added to cells in log phase to a final
530 concentration of 250 ng/mL. Samples collected at time points indicated in the figure
531 legend were prepared for extraction of RNA for RT-qPCR.

532 To block the vacuolar degradation of Atg39-pHn-mCh by treatment with PMSF,
533 PMSF (in DMSO) was added to cells in log phase to a final concentration of 1mM.

534

535 ***Yeast strain construction***

536 All strains used in this study are listed in Supplementary Table 1. PCR-based
537 methods[69] using the pFA6a[70] and pK3F[71] plasmid series as templates were used to
538 generate genomic integration cassettes of sequences encoding fluorescent protein
539 genes and to delete ORFs at the genomic loci[72]. To generate PMCPL576, the *mEGFP*
540 gene followed by a kanamycin resistance cassette (*KAN-MX6*) flanked by loxP sites
541 was amplified from pPM09 using primers with homology arms that are complementary
542 to flanking sequences of the region targeted for genomic insertion. The PCR product
543 was transformed into W303A and kanamycin-resistant colonies were selected. A colony
544 containing the *KAN-MX6* cassette integrated into the proper location as assessed by
545 PCR of genomic DNA was transformed with the centromeric plasmid pSH47[73] that
546 expresses the Cre recombinase under the control of a galactose-inducible (*GAL1*)
547 promoter. Transformants were selected on csm plates lacking uracil (ura). Overnight
548 cultures of individual colonies grown in csm -ura supplemented with 2% raffinose were
549 diluted into csm -ura supplemented with 2% galactose to induce the expression of the
550 Cre recombinase for 5 hours before single cells were plated on YPD. Colonies were
551 screened for loss of *KAN-MX6* by testing growth on geneticin (Thermo Fisher
552 Scientific)-containing plates; the expression of *ATG39-mEGFP* was confirmed by
553 fluorescence microscopy and immunoblot. PMCPL578, PMCPL1257, PMCPL1045, and
554 PMCPL1097 were generated in a similar manner using pPM26, pPM31, pPM28, and
555 pPM27 respectively as PCR templates.

556 Genomic integration of *DNM1* and *dnm1 K41A* genes (PMCPL1319,
557 PMCPL1087, PMCPL1112, and PMCPL1113) were generated by genomically
558 integrating linearized pPM11 and pPM15 at the *URA3* locus.

559

560 ***Plasmid generation***

561 All plasmids used in this study are listed in Supplementary Table 2. All DNA
562 fragments used for cloning were purified using a gel purification kit/protocol (Qiagen). All
563 PCR was performed using KOD polymerase (EMD Millipore). To generate pPM09,
564 pPM27, and pPM32, the *mEGFP*, *pHluorin*, and *mCherry* ORFs were amplified by PCR
565 using pFa6a-mEGFP-kanMX6 (a gift from Julien Berro[74], Addgene plasmid # 87023),
566 pAS1NB (a gift from Mark Prescott[37], Addgene plasmid # 71245), and pFa6a-3xHA-
567 mCherry-natMX6, respectively. The amplicons were then assembled into pK3F
568 (linearized with *Spe*I (New England Biolabs)) using the Gibson Assembly Master Mix
569 (New England Biolabs). pPM28 was similarly generated by Gibson Assembly of the
570 *pHluorin* amplicon into pPM32. To generate pPM31, the ORF for *hfYFP*[64] was yeast
571 codon optimized using the codon optimization tool from IDT and synthesized as a g-
572 block flanked by *Spe*I restriction enzyme recognition sites (IDT). The g-block was
573 solubilized in TE and Gibson Assembled into pK3F as described above. To generate
574 pPM29, an amplicon containing the *HEH1* promoter, the coding sequence of a fragment
575 of Heh1 encoding the first 479 amino acids, followed by the *ADH1* 3'UTR, was amplified
576 by PCR using genomic DNA from PMCPL1082 as a template and primers with *Eag*I and
577 *Xho*I restriction enzyme recognition sites. The amplicon was restriction digested with
578 *Eag*I (New England Biolabs) and *Xho*I (New England Biolabs) and ligated (T4 DNA
579 ligase, Invitrogen) into pRS405 digested with *Eag*I and *Xho*I. To generate pPM30, an
580 ORF containing the mCherry coding sequence was generated by PCR using pSJ1321
581 (a gift from Sue Jaspersen[75], Addgene plasmid #86413) as a template and primers with

582 *BamH*I and *Pac*I restriction enzyme recognition sites. The amplicon was restriction
583 digested with *BamH*I (New England Biolabs) and *Pac*I (New England Biolabs) and
584 ligated into gel purified pPM29 digested with *BamH*I and *Pac*I.

585 pPM03 was generated in two steps. First, the genomic region containing the
586 *ATG8* promoter (576 base pairs immediately upstream of the *ATG8* start codon) was
587 generated by PCR using genomic DNA from W303A and primers with *Sac*I and *Eag*I
588 restriction enzyme recognition sites. The amplicon was restriction digested with *Sac*I
589 (New England Biolabs) and *Eag*I ligated into pRS406 linearized with *Sac*I and *Eag*I.
590 Next, the genomic region containing the *ATG8* terminator (319 base pairs immediately
591 downstream of the *ATG8* stop codon) was generated in a similar manner using primers
592 with *Hind*III and *Sal*I restriction enzyme recognition sites. The amplicons were digested
593 with *HindIII* and *SalI* ligated into the plasmid containing the *ATG8* promoter linearized
594 with *Hind*III (New England Biolabs) and *Sal*I (New England Biolabs). To generate
595 pPM11, the *DNM1* gene was amplified by PCR using genomic DNA from W303A and
596 primers with *Eag*I and *Spe*I restriction enzyme recognition sites. The amplicon was
597 restriction digested with *Eag*I and *Spe*I and ligated into pPM03 linearized with *Eag*I and
598 *Spe*I.

599 To generate pPM15, site-directed mutagenesis of the codon encoding lysine at
600 amino acid position 41 was altered to alanine using the Q5 site-directed mutagenesis kit
601 (New England Biolabs) using pPM11 as a template. All plasmid sequences were
602 confirmed by Sanger sequencing.

603

604 ***RTqPCR***

605 RNA extraction was performed using the MasterPure Yeast RNA purification kit
606 (Lucigen) from samples treated as indicated in the legend of Figure S1. cDNA was
607 produced from ~1 µg of RNA using M-MuLV Reverse Transcriptase (New England
608 Biolabs). RTqPCR was performed on 1:10 dilutions of the cDNA using iTaq Universal
609 SYBR Green Supermix (Bio Rad) and primer pairs validated for RTqPCR efficiency for
610 *ATG39* (sATG39 qPCR 6 and asATG39 qPCR 6), *ATG8* (sATG8 qPCR and asATG8
611 qPCR), *ATG11* (sATG11 qPCR and asATG11 qPCR), *ATG40* (sATG40 qPCR and
612 asATG40 qPCR), and *ACT1* (sACT1 qPCR and asACT1qPCR) which served as a
613 control. All PCRs were performed using CFX96 Touch Real-Time Detection System
614 thermocycler (BioRad). Cq values as reported by the thermocycler during the RTqPCR
615 for the gene of interest were subtracted from those of *ACT1* to obtain ΔCq. ΔΔCq was
616 then obtained by subtracting the ΔCq value of the control condition from the condition of
617 interest (i.e. rapamycin or nitrogen starvation). Fold change was calculated as $2^{-\Delta\Delta Cq}$.

618

619 ***Live-cell Microscopy***

620 For all live-cell imaging, cells incubated in sd-N for the duration of time indicated
621 in the figure legend were gently collected by centrifugation and resuspended in sd-N
622 medium prior to imaging. Images from Figure 1C, Figure S1F, Figure S2D, and the
623 images used to generate the data in Figure 3D were acquired on a DeltaVision
624 microscope (Applied Precision) equipped with a UPlanSapo x100 1.4 numerical
625 aperture oil immersion objective (Olympus), and an AURA light engine (Lumencor) and
626 CoolSnapHQ^2 charge-coupled device (CCD; Photometrics) camera imaging using an
627 Insight SSI four-color live-cell filter set (GFP: excitation, 425–495 nm and emission,

628 500–550 nm; YFP: excitation, 496–528 nm and emission, 537–559 nm; mCherry:
629 excitation, 555–590 nm and emission, 600– 675 nm) using Resolve3D in SoftWoRx
630 7.0.0 software. The microscope stage and objectives were maintained at 30°C within an
631 environmental chamber.

632 All other images were acquired on a lattice light sheet microscope[76] equipped
633 with a 25X 1.1 numerical aperture CFI APO LWD objective (Nikon) whose focal plane is
634 coincident with the light sheet, and a sCMOS camera (Hamamatsu Orca Flash 4.0 v2).
635 Cells were added to 5 mm round cover slips (Warner Instruments) coated with
636 Concanavalin A (Sigma) as described in[77]. The coverslip with the cells adhered was
637 then placed in an imaging chamber in a bath containing sd-N medium warmed to 30°C.

638

639 ***Correlative light and electron microscopy***

640 Correlative light and electron microscopy of resin-embedded cells was performed
641 based on the protocol published by Kukulski and colleagues[78]. In brief, cells
642 (PMCPL1283 and PMCPL1390) were cultured in sd-N for four hours. Cells were
643 pelleted by centrifugation at ~800 RCF for five minutes and high-pressure frozen in the
644 200-µm recess of an aluminum platelet (Engineering Office M. Wohlwend 241) using an
645 HPM100 (Leica Microsystems). The samples were then freeze substituted in 0.1%
646 uranyl acetate. Automated temperature control was then used to complete the solution
647 exchange and embedding in Lowicryl HM20 (Polysciences). Sectioning was performed
648 using a diamond knife (Diatome) mounted on an ultramicrotome (Leica Artos 3D) to a
649 nominal thickness of 250 µm. Sections were then collected on carbon-supported 200-
650 mesh copper grids (Ted Pella 01840).

651 The position of Atg39-hfYFP was determined by fluorescence microscopy. Next,
652 15 nm protein A-coated gold beads (Cell Microscopy Core, University Medical Center
653 Utrecht) were adhered to the grids to aid in the tilt-series alignment.

654 We used automated tilt-series acquisition via SerialEM 3.6.15[79] on an electron
655 microscope (FEI TF20) operating at 200 kV from approximately -65 to +65 degrees
656 (one-degree increments) with a high-tilt tomography holder (Fischione Instruments
657 2020), a 100 µm objective aperture, a 150 µm C2 aperture, and a 4k x 4k Eagle CCD
658 (FEI) at a binned pixel size of 1.242 nm. Single- or dual-axis tilt series were acquired as
659 necessary to achieve sufficient contrast to visualize membranes. IMOD 4.11.24[80] was
660 used for reconstruction (in an automated fashion[81]), nonlinear anisotropic diffusion
661 filtering, and manual segmentation. Vph1-3xHA-mCherry and Nup170-mCherry
662 fluorescence were used to correlate fluorescence and electron microscopy images to
663 localize the Atg39-hYFP within the ultrastructure.

664

665 ***Calculating expected time resolution in observable morphological intermediates***
666 ***in CLEM***

667 A modification of the popular coupon collector's problem[82] from probability theory
668 was used to estimate the number of tomograms needed to observe all morphologies in
669 nucleophagy which persist for a given amount of time. The equation used is

672 $$\boldsymbol{E} = \frac{\boldsymbol{T}}{\Delta \boldsymbol{t}}\left(\frac{\mathbf{1}}{\mathbf{1}} + \frac{\mathbf{1}}{\mathbf{2}} + \cdots + \frac{\mathbf{1}}{\boldsymbol{T}/_{\Delta \boldsymbol{t}}}\right)$$

670 where E is the expected number of tomograms need to visualize at least one example
671 of all morphological intermediates that exist for a time (Δt) as a ratio to the average time

673 (T) Atg39- foci are outside of the vacuole (~300 seconds, Figure 3I). Using this formula,
674 we calculated that 30 tomograms were sufficient to achieve a time resolution of 30
675 seconds. Simply put, it is statistically likely to observe at least one instance of a
676 morphological intermediate in nucleophagy that is identifiable by CLEM that persists for
677 more than 30 seconds in a random selection of 30 tomograms.

678

679 ***Image processing and analysis***

680 Micrographs acquired on the Applied Precision DeltaVision microscope were
681 deconvolved using an iterative algorithm in SoftWoRx (6.5.1; Applied Precision, GE
682 Healthcare). Unprocessed images were used for all quantification of fluorescence
683 intensity on micrographs acquired on the DeltaVision. Fluorescence intensity values
684 from micrographs were measured in FIJI/imageJ[83]. Micrographs acquired on the LLSM
685 were deskewed and deconvolved as described in[76]. LLSM images were rendered in 3D
686 (Figure 3A and 3B) using the commercial software Imaris (Oxford Instruments).

687

688 ***Nucleophagic flux calculations***

689 Cells expressing Atg39-pHluorin-mCherry (PMCPL1045, PMCPL1078,
690 PMCPL1079, PMCPL1253, PMCPL1130, PMCPL1282, PMCPL1066, PMCPL1249,
691 PMCPL1276, PMCPL1243, PMCPL1252, PMCPL1264, PMCPL1067, PMCPL1127,
692 PMCPL1293, PMCPL1274, PMCPL1124, PMCPL1421, PMCPL1430, PMCPL1443,
693 PMCPL1493, PMCPL1496) were cultured overnight, incubated in sd-N media for 6
694 hours, and prepared for imaging on the DeltaVision. To calculate nucleophagic flux, all

695 the Atg39-pHluorin-mCherry foci in the cell were manually counted and the number of
696 red-only foci was divided by the sum of the red-only and red/green foci. The ratio
697 obtained in WT was normalized to 1 and used to compare to all other genotypes.

698

699 ***NE mCherry fluorescence calculation***

700 Cells expressing Atg39-pHluorin-mCherry (PMCPL1045, PMCPL1078,
701 PMCPL1079, PMCPL1253, PMCPL1130, PMCPL1282, PMCPL1066, PMCPL1249,
702 PMCPL1276, PMCPL1243, PMCPL1252, PMCPL1264, PMCPL1067, PMCPL1127,
703 PMCPL1293, PMCPL1274, PMCPL1124, PMCPL1421, PMCPL1430, PMCPL1443,
704 PMCPL1493, PMCPL1496) were cultured overnight, incubated in sd-N media for 6
705 hours, and prepared for imaging on the DeltaVision. To measure NE mCherry
706 fluorescence, a 4 pixel-wide ROI was drawn along the nuclear periphery in regions
707 devoid of Atg39 foci and the mean fluorescence intensity was measured and
708 background fluorescence was subtracted.

709

710 ***Nucleophagy frequency quantification***

711 The number of Atg39-GFP accumulations in an experiment (three biological
712 replicates total) was divided by the total number of cells. The resulting number was then
713 divided by the duration of the experiment to obtain the number of nucleophagic
714 events/cell/hour.

715

716 ***Determining Atg39-GFP copy number***

717 Atg39-GFP expressing cells (PMCPL940, PMCPL856) were incubated in sd-N
718 media for four hours prior to imaging and each were separately mixed with Fta3-GFP
719 expressing cells (MKSP3186) and mounted onto coverslips. Raw images were then
720 analyzed using a custom-written MATLAB function, 'findIrregularSpots3' described
721 previously[60] that finds fluorescent objects regardless of their shape and returns xyz-
722 coordinates of the object centroids. The xyz coordinates were then used as inputs for a
723 custom-written MATLAB function 'fitSpots3' to fit and compute the volume of a 2D
724 Gaussian to a Z-slice image closest to the z-coordinate of the spot centroid. Fta3-GFP
725 spots were manually curated for their position in the cell cycle and those that were
726 determined to be in anaphase B were selected for analysis. Atg39-GFP copy number
727 was estimated by dividing the Gaussian volume for each spot by the average Gaussian
728 volume of the Fta3-GFP spots, previously calculated to be 111 molecules[63]. Fta3-GFP
729 foci identified as outliers using ROUT test Q=1%, one iteration, were excluded.

730

731 ***Particle tracking/colocalization***

732 Cells (PMCPL940, PMCPL857, PMCPL831, PMCPL832, PMCPL840,
733 PMCPL1319, PMCPL1320, and PMCPL1087) were incubated in sd-N media for three
734 hours before being prepared for imaging on the LLSM. Cells where a Atg39-GFP focus
735 appeared that underwent nucleophagy were selected for further processing using
736 MATLAB scripts to detect Atg39-GFP foci (spots) as described in "Determining Atg39-
737 GFP copy number." For particle tracking and colocalization analysis the spots were
738 organized into trajectories using previously described MATLAB implementation[61] of the
739 widely-used tracking algorithm 'track.m'[62]. Trajectories of a single Atg39-GFP spot that

740 were erroneously split in two (when displacement between two frames exceeded a
741 maximum linking distance) were linked together manually. For the relative spot intensity
742 analysis, Gaussian volumes were calculated from Atg39-GFP spots as described
743 above. The Gaussian volume of the tracked spot was normalized to that of the first time
744 point in the trajectory. The spot coordinates in each track were also used to calculate
745 displacement of Atg39-GFP between frames using a custom Jupyter Notebook script,
746 implemented in Python (Figure 3E,G, Figure S2C).

747 For colocalization analysis, a custom Jupyter Notebook Python script used the
748 coordinates of the identified Dnm1-mCherry spots which correspond to the time points
749 of the Atg39-GFP tracks to calculate the distance from the center of the Atg39-GFP
750 spots to the center of the closest Dnm1-mCherry spot (Figure 2D,E, Figure S2A,B). For
751 all time points in which the distance between Atg39-GFP and Dnm1-mCherry spots
752 were calculated to be 400 nm or less, a small ROI around the Atg39-GFP spot was
753 cropped and the Pearson's correlation coefficient between the two channels was
754 determined using the Fiji plugin JaCoP[84]. The particles were considered colocalized if
755 the Pearson's correlation coefficient was >0.5.
756 All MATLAB and Jupyter Notebook Python script are available on GitHub.

757

758 ***Quantification of INMDV diameter***

759 The diameter of the INMDVs was measured in IMOD.

760

761 ***Estimation of the percentage of INM turned over by nucleophagy in 24 hours***

762 To estimate the percentage of INM that could be turned by nucleophagy in 24
763 hours, the amount of surface area of the INMDV removed in one round of nucleophagy
764 in WT cells was determined. For this, the surface area of INMDVs in category 2-4 (i.e.
765 after release as cytosolic NDVs) were approximated as ellipsoids and the length of the
766 major and minor axes were measured on IMOD. The a and b axes (major and minor
767 axes) were measured as the maximum distance within the membrane of the INMDV
768 and the distance within the membrane orthogonal to the maximum, respectively. The c
769 axis was recorded as the distance between the intersection of the major and minor axes
770 and the edge of the INMDV. The surface area was then approximated using the a, b,
771 and c radii and the ellipsoid surface area formula. The median value was then multiplied
772 by the frequency of nucleophagy (1.4 events/cell/hour) and by 24 hours to estimate the
773 surface area of the of INM removed per cell in 24 hours. This value was calculated as
774 ~7.14 μm^2. To estimate the surface area of the NE prior to nitrogen starvation, cells
775 expressing Heh1-GFP were imaged in log phase, and the radii of the nuclei were
776 measured, and the surface area was calculated using the equation for the surface area
777 of a sphere. The mean value was determined to be ~8.63 μm^2.

778

779 ***Statistical methods***

780 Graphs were generated using Prism (GraphPad 9.0). Where relevant, we used
781 an appropriate experimental group that was carrier treated as a reference to test for
782 contribution of other covariates. Statistical significance tests were used as indicated in
783 figure legends. Significance values were calculated within Prism (GraphPad 10.0) and
784 p-values are indicated on the graph or in figure legends as: *ns*, $p > 0.05$; * $p \leq 0.05$; ** p

785 ≤ 0.01; *** $p \leq 0.001$; **** $p \leq 0.0001$. All data was assumed to be normal with equal
786 variance. Error bars are described in figure legends.

787

788 ***Whole cell extract preparation***

789 5 O.D. cells were pelleted by centrifugation and resuspended in 10% TCA for 1 h
790 on ice and centrifuged at 15,000 *g* for 10 min at 4°C. The pellet was washed with ice-
791 cold acetone, homogenized by sonication (Bioruptor UCD-200) and pelleted by
792 centrifugation. After two cycles of washing and sonication, the pellet was vacuum-dried
793 for 15 min. The dried cell pellet was then mechanically disrupted with 100 µl glass
794 beads (Sigma) and 100 µl 50 mM Tris-HCl pH 7.5, 8 M urea, 2% SDS, and 1 mM EDTA,
795 followed by addition of 100 µl protein sample buffer (Tris-HCl pH 6.8, 7 M urea, 10%
796 SDS, 24% glycerol, bromophenol blue, and 10% β-mercaptoethanol).

797

798 ***Immunoblotting***

799 Proteins from whole cell extracts were resolved on 4-20% SDS-polyacrylamide
800 gels (BioRad), followed by transfer of the proteins to 0.2 µm nitrocellulose membranes
801 (Bio-Rad). The membranes were blocked in 5% non-fat milk in TBST for 1 h and
802 immunoblotted with an antibody against HA directly conjugated to HRP (anti-HA-HRP;
803 Roche) for 1 h at room temperature or with an antibody against GFP (anti-GFP;
804 Biolegend) overnight at 4°C. Blots incubated with anti-GFP were then incubated with a
805 secondary antibody against mouse (anti-mouse-HRP; Invitrogen) for 1 h at room
806 temperature. Blots were visualized by ECL (Thermo Fisher Scientific) using a VersaDoc

807 Imaging System (BioRad). Relative protein loading was visualized using Ponceau S
808 Solution (Sigma).

809 **Data Availability**

810 Source data will be provided with this paper at the time of publication. All other
811 data supporting the findings presented in this study are available from the
812 corresponding author upon reasonable request.

813 **Code Availability**

814 The MATLAB and Jupyter Notebook Python scripts are available with no access
815 restrictions at https://https://github.com/LusKingLab/.

816

Supplemental Figures

Figure S1

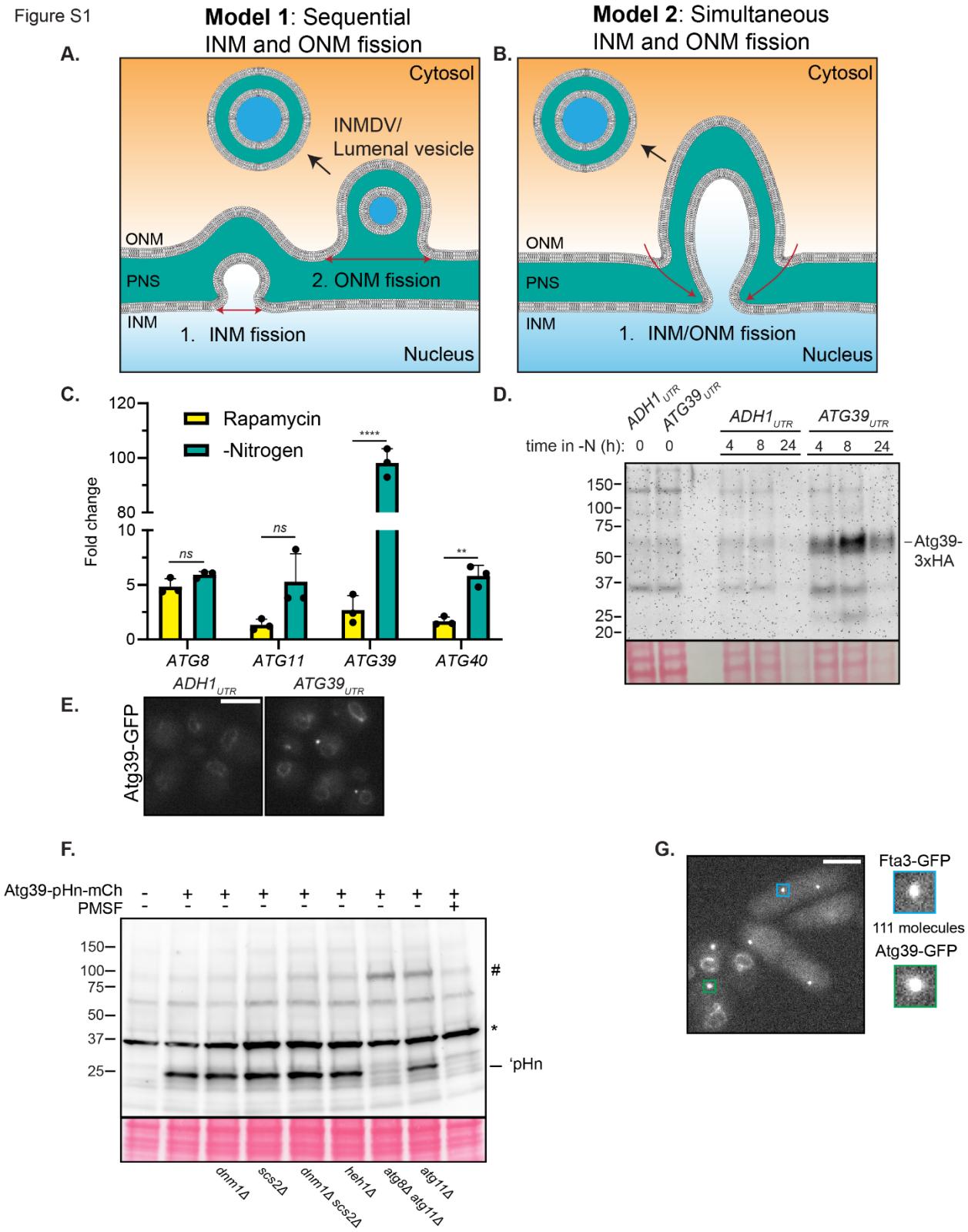

Supplemental Figure 1 – Models of nucleophagy and characterization of Atg39 expression and copy number.

A,B) Schematic of two models of nucleophagy incorporating either sequential (Model 1) or simultaneous (Model 2) INM and ONM fission events. Model 1 would also lead to the formation of a lumenal vesicle/INMDV intermediate. ONM, outer nuclear membrane; INM, inner nuclear membrane; PNS, perinuclear space; INMDV, inner nuclear membrane-derived vesicle; NDV, nucleus-derived vesicle.

C) RTqPCR on indicated autophagy gene transcripts was performed in WT cells either treated with rapamycin for 2 h or cultured in medium lacking nitrogen for 2 h. Results displayed as a bar graph comparing the mean fold change of the transcripts between the rapamycin and -Nitrogen condition. Mean and standard deviation (error bars) of three biological replicates (black dots). Unpaired two-sided t tests. ****P<0.0001; **P<0.01; *ns*, not significant.

D) Protein levels of Atg39-3xHA fusions derived from transcripts including either the *ADH1* 3'UTR or the endogenous *ATG39* 3'UTR were assessed by western blot with anti-HA antibody directly coupled to HRP (α-HA-HRP) and ECL. Positions of molecular weight standards (kD) at left. At bottom, membranes were stained with Ponceau to evaluate total protein loads.

E) Fluorescence micrographs of Atg39-GFP produced from transcripts with 3'UTRs from the *ADH1* or *ATG39* genes after 4 h in medium lacking nitrogen. Scale bar is 5 µm.

F) Western blot of whole protein extracts from cells expressing Atg39-pHn-mCh with fall out fragment ('pHn) in the indicated genetic backgrounds and PMSF treatment after 24 h in sd-N. Position 'pHn indicated on the right. An anti-GFP antibody and anti-mouse-HRP secondary followed by ECL was used to detect proteins. Positions of molecular weight standards (kD) at left. * is a non-specific band. # is the expected position of Atg39-pHn-mCh, which is undetectable in most backgrounds due to its low abundance and lack of sensitivity of the anti GFP antibody.

G) To calculate copy number of Atg39-GFP within individual foci, we imaged budding yeast expressing Atg39-GFP next to *S. pombe* expressing Fta3-GFP, a kinetochore protein which has 111 molecules/focus in anaphase B[60]. By directly relating the fluorescence intensities, we calculated Atg39-GFP copy number/focus as presented in Figure 3D.

818

Figure S2

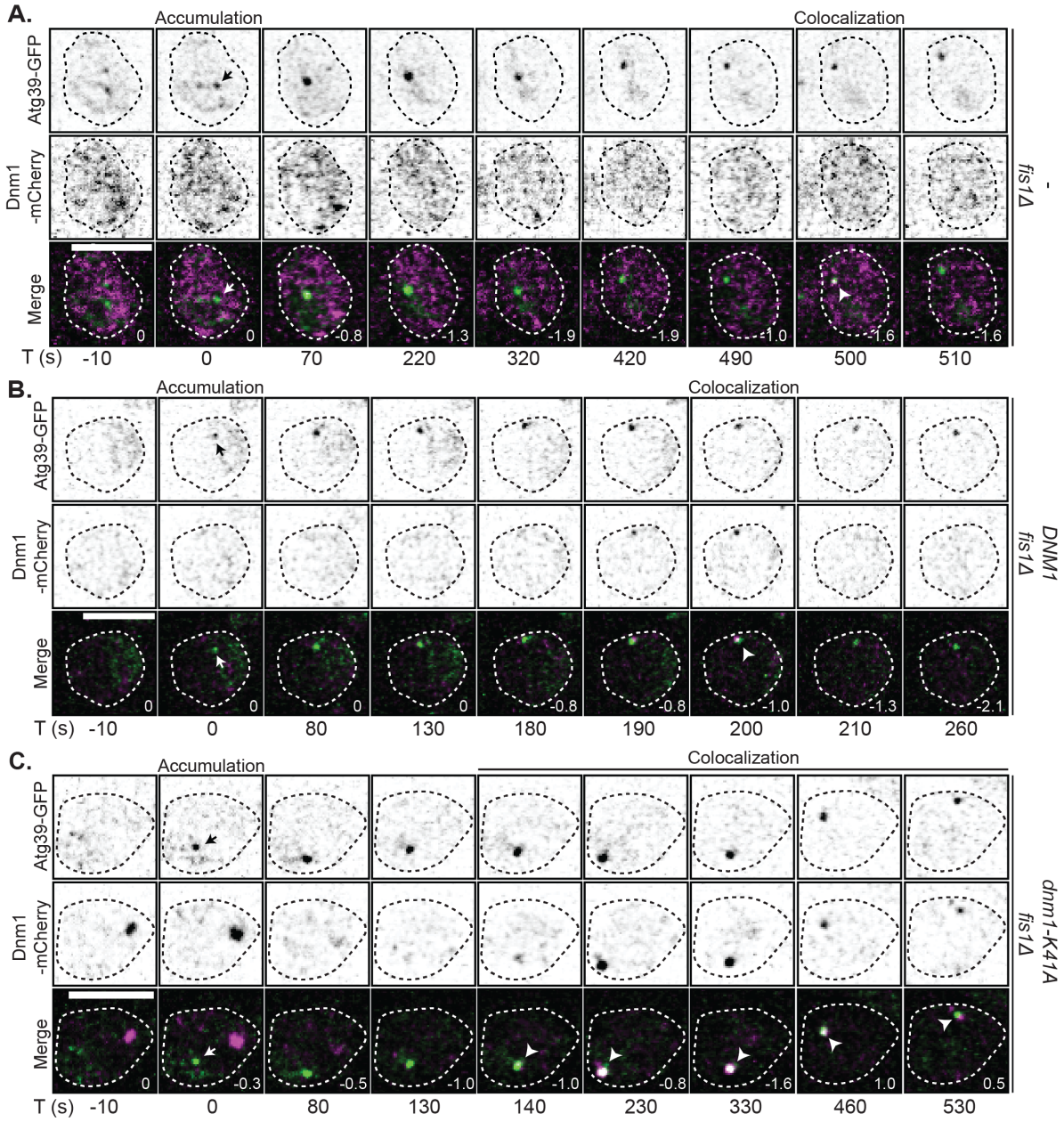

819

Supplemental Figure 2 – Dnm1 colocalizes with Atg39 in the absence of Fis1.

A-C) Inverted fluorescence micrographs of a timelapse series of *fis1Δ* cells expressing Atg39-GFP and Dnm1-mCherry with and without either an extra copy of *DNM1* or the dominant negative *dnm1-K41A* allele under conditions of nitrogen starvation. Green and red channels shown with merge at indicated times (T) with T=0 s being the first detection of a Atg39-GFP focus (arrow). Arrowheads point to colocalization between Atg39-GFP and Dnm1-mCherry. Numbers in merge are the z-position (in µm) of the image shown in reference to the midplane. Scale bars are 5 µm.

Figure S3

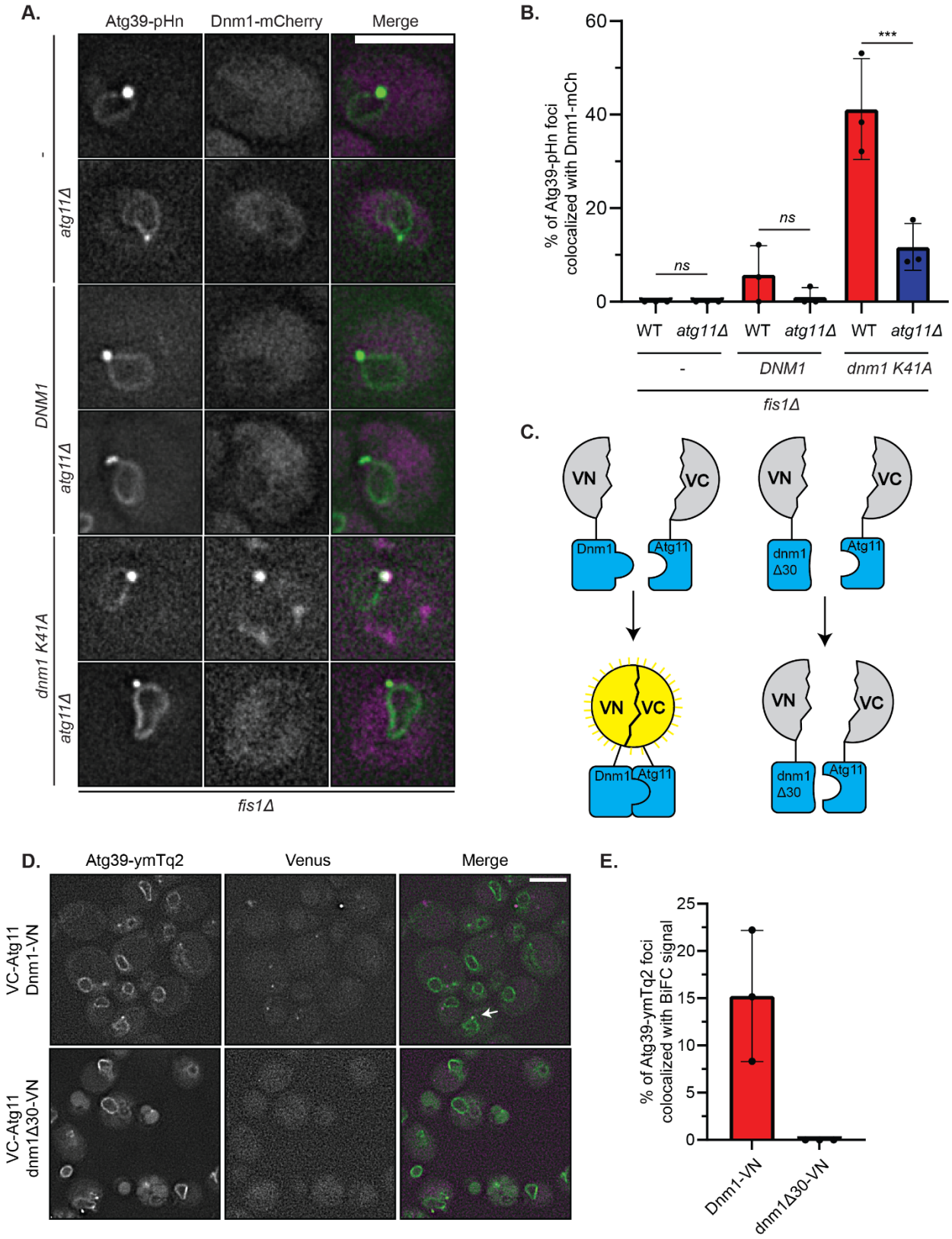

820

Supplemental Figure 3 – Atg11 recruits Dnm1 to the NE.

A) Fluorescence micrographs of *fis1Δ* cells and *fis1Δatg11Δ* cells expressing Atg39-pHn, Dnm1-mCherry with and without an extra copy of *DNM1* or the *dnm1-K41A allele* under conditions of nitrogen starvation. Green and red channels shown with merge. Scale bar is 5 μm.

B) Plot of the mean percentage of Atg39-pHn foci that colocalize with Dnm1-mCherry from experiments in **A**. Mean and standard deviation (error bars) from three biological replicates (black dots). For *fis1Δ* cells, *n*=79 Atg39-pHn foci. For *fis1Δ* cells expressing *DNM1*, *n*=104 Atg39-pHn foci. For *fis1Δ* cells expressing *dnm-K41A*, *n*=166 Atg39-pHn foci. For *fis1Δ atg11Δ* cells, *n*=78 Atg39-pHn foci. For *fis1Δatg11Δ* cells expressing *DNM1*, *n*=96 Atg39-pHn foci. For *fis1Δatg11Δ* cells expressing *dnm1-K41A*, *n*=165 Atg39-pHn foci. Unpaired two-sided t test. ***P<0.001; *ns*, not significant.

C) Schematic of BiFC. VN and VC are the N- and C- terminal fragments of Venus, respectively. An interaction between Dnm1-VN (but not dnm1Δ30) and Atg39-VC leads to the reconstitution of Venus and its fluorescence.

D) Fluorescence micrographs of cells expressing Atg39-ymTurquoise2 (Atg39-ymTq2), VC-Atg11, and either Dnm1-VN or dnm1Δ30-VN under conditions of nitrogen starvation. Yellow (magenta) and blue (green) channels shown with merge. The arrow points out colocalization between the Venus and Atg39-ymTq2 foci. Scale bar is 5 μm.

E) Plot of the mean percentage of Atg39-ymTq2 foci that colocalize with Venus foci from experiments in **D**. Mean and standard deviation (error bars) from three biological replicates. For cells expressing Dnm1-VN, *n*=84 Atg39-ymTq2 foci. For cells expressing dnm1Δ30-VN, *n*=93 Atg39-ymTq2 foci.

821

Figure S4

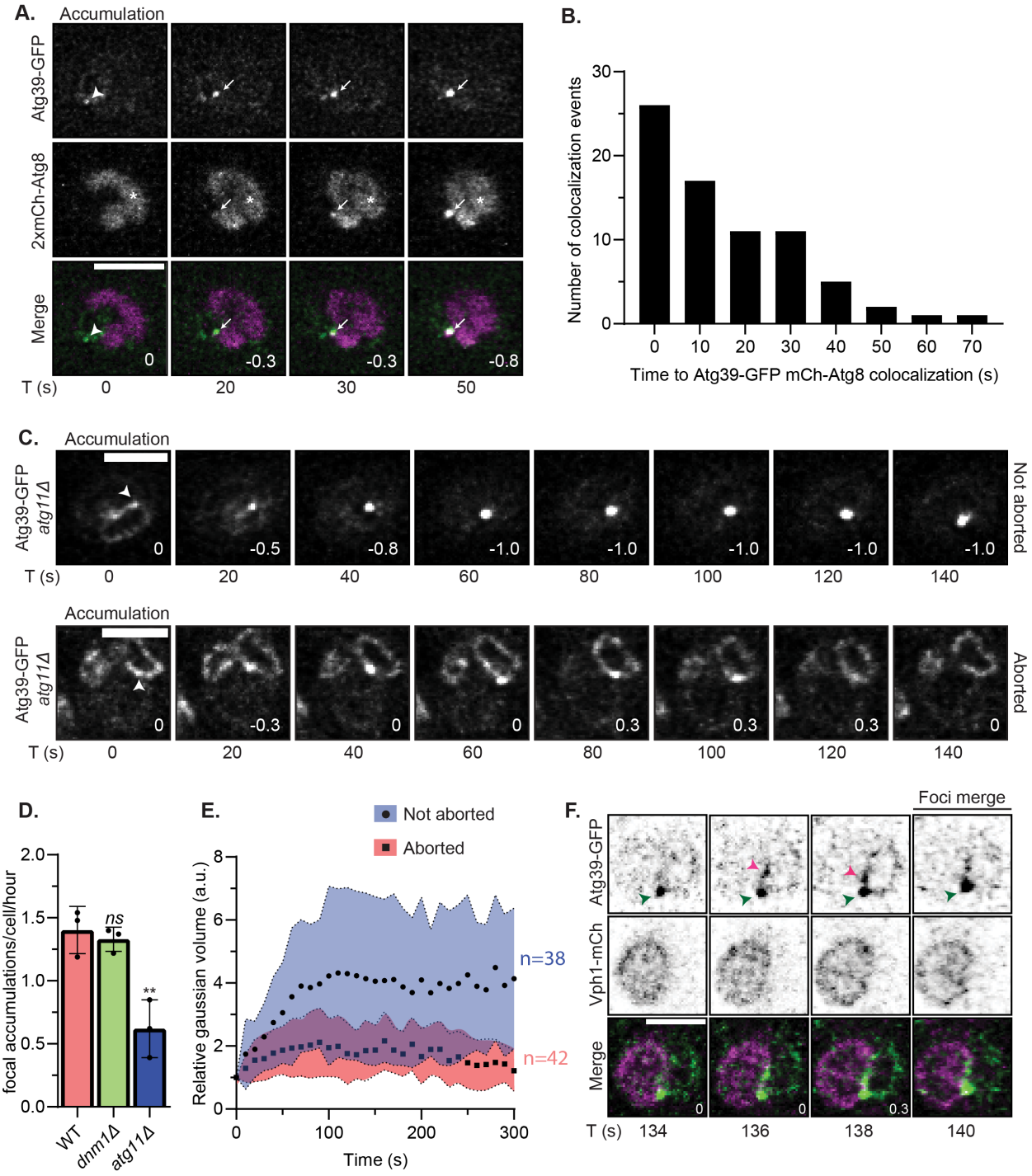

822

Supplemental Figure 4 – Atg8 recruitment, Atg11 dependence, and Atg39 dynamics during nucleophagy.

A) Fluorescence micrographs of cells expressing Atg39-GFP and 2xmCherry(mCh)-Atg8 imaged every 10 seconds under conditions of nitrogen starvation. Green and red channels shown with merge. Numbers in merge are z-position (in µm) of the displayed image in reference to the midplane. T (s) indicates the time in seconds since the first detection of the Atg39-GFP focus (indicated above, arrowhead). Arrows point to colocalization between Atg39-GFP and 2xmCh-Atg8. * indicates fluorescence from the vacuole in the red channel. Scale bar is 3 µm.

B) Histogram of the number of colocalization instances for the indicated time after the appearance of an Atg39-GFP focus. Data are from the experiments in **A**; *n*=73 cells, 74 tracks, three biological replicates.

C) Fluorescence micrographs of *atg11Δ* cells expressing Atg39-GFP, Vph1-mCherry, and Nup170-mCherry every 10 seconds under conditions of nitrogen starvation. Green channel is shown. Numbers in merge are z-position (in µm) of the displayed image in reference to the midplane. T (s) indicates the time in seconds since the first detection of the Atg39-GFP focus (indicated above, arrowhead). Cells shown are representative examples from the two groups of tracks in which the Atg39-GFP focus disappears prior to internalization in the vacuole (aborted) or not (not aborted).

D) Plot of the mean number of focal accumulations divided by the total number of cells divided by the total time of the experiment (h) for the indicated genotype. Data are from three biological replicates (black dots). For WT cells, *n*=294 cells. For *dnm1Δ* cells, *n*=557 cells. For *atg11Δ* cells, *n*=522 cells. Ordinary one-way ANOVA with multiple comparisons with **P<0.01; *ns*, not significant.

E) Fluorescence intensity of Atg39-GFP foci in *atg11Δ* cells plotted versus time after their first detection. Data are split into two groups, aborted (red, squares) and not aborted (blue, circles) from three biological replicates. For cells in the aborted group, *n*=40 cells, 42 tracks. For cells in the not aborted group, *n*=37 cells, 38 tracks.

F) Inverted fluorescence micrographs of WT cells expressing Atg39-GFP and Vph1-mCherry (mCh) imaged every two seconds under conditions of nitrogen starvation. Green and red channels shown with merge. Numbers in merge are z-position (in µm) of the displayed image in reference to the midplane. T (s) indicates the time in seconds since the first detection of the Atg39-GFP focus (green arrowhead). Another less intense focus of Atg39-GFP is visible merging with the initial particle (pink arrowhead). Scale bar is 3 µm.

823

Figure S5

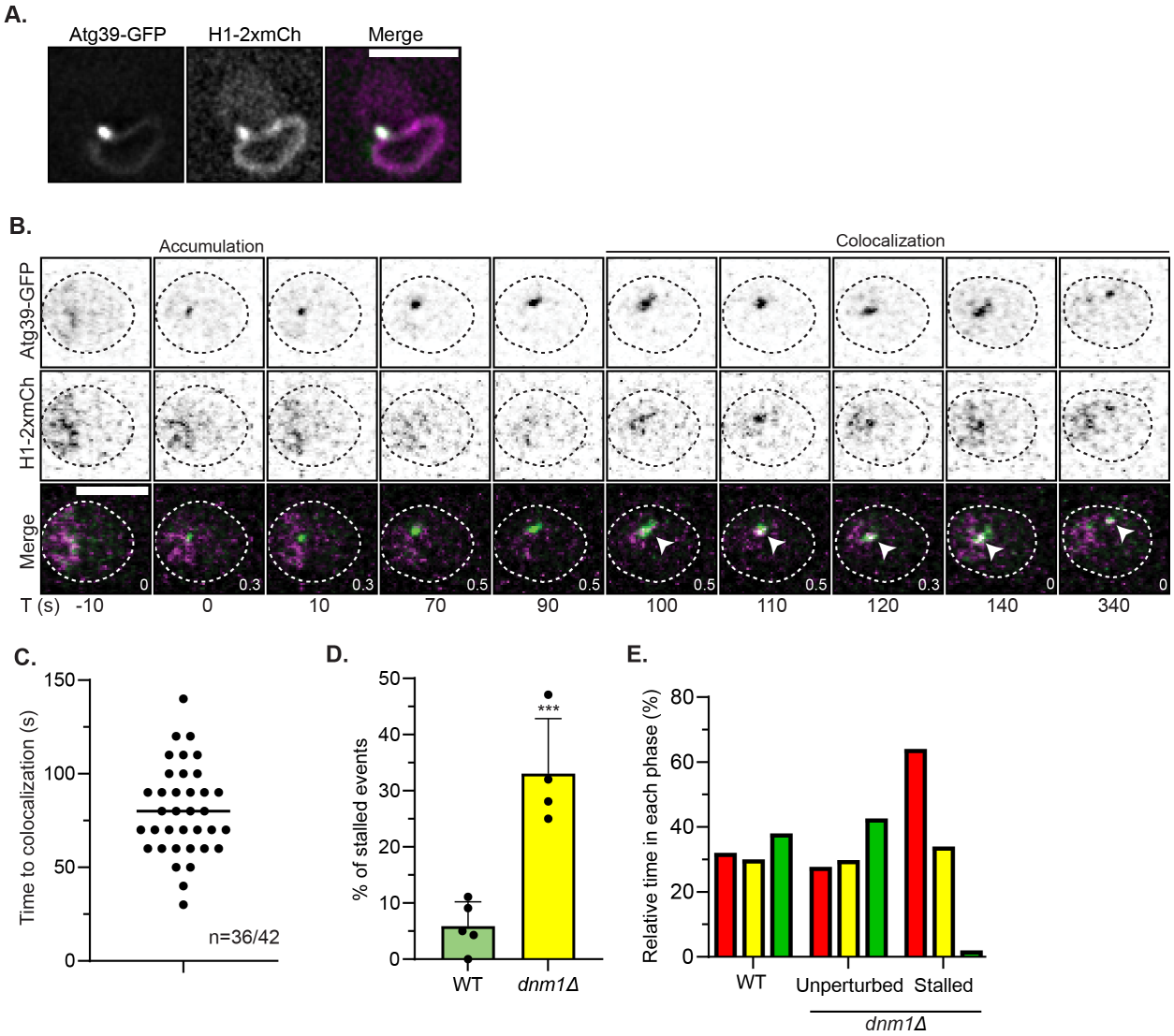

824

Supplemental Figure 5 – Characteristics of Atg39-GFP mobility and cargo capture.

A) Fluorescence micrographs of WT cells expressing Atg39-GFP and a model INM cargo comprising the INM targeting and transmembrane domain of Heh1 fused to two tandem mCherry fluorophores (H1-2xmCh) under conditions of nitrogen starvation. Green and red channels shown with merge. Scale bar is 3 µm.

B) Inverted fluorescence micrographs of WT cells expressing Atg39-GFP and H1-2xmCh under conditions of nitrogen starvation. Imaged every 10 seconds with time 0 assigned to the point of Atg39-GFP focal accumulation. Green and red channels shown with merge. Arrowheads point to colocalization between Atg39-GFP and H1-2xmCh. Cell boundaries are outlined. Numbers in merge are z-position (in µm) of the displayed image in reference to the midplane. Scale bar is 3 µm.

C) Scatter plot depicting the elapsed time from the first detection of an Atg39-GFP focus and the first instance of colocalization with H1-2xmCh from experiments as in **B**. The median is depicted by a black bar. *Data are from n=36 cells in which Atg39-GFP and H1-2xmCh were found colocalized outside of the nucleus out of n=42 total cells from two biological replicates.*

D) Bar graph of the percentage of Atg39 foci tracked from first appearance that never make it into the vacuole over a 20-minute timelapse experiment as noted in Figure 3F for the indicated genotype. Mean and standard deviation (error bars) from 5 (WT cells) or 4 (*dnm1*Δ cells) biological replicates (black dots). Unpaired two-sided t test, *n*=114 tracks, 99 cells for WT cells and *n*=95 tracks, 82 cells for *dnm1*Δ cells. ***P<0.001.

E) Plot of the fraction of time (as a percentage) that Atg39-GFP particles spend in each phase as per color code in Figure 3E and 3G in WT and *dnm1Δ* cells. The latter are also segregated based on those that enter the vacuole (unperturbed) and those that don't (stalled).

825

Figure S6

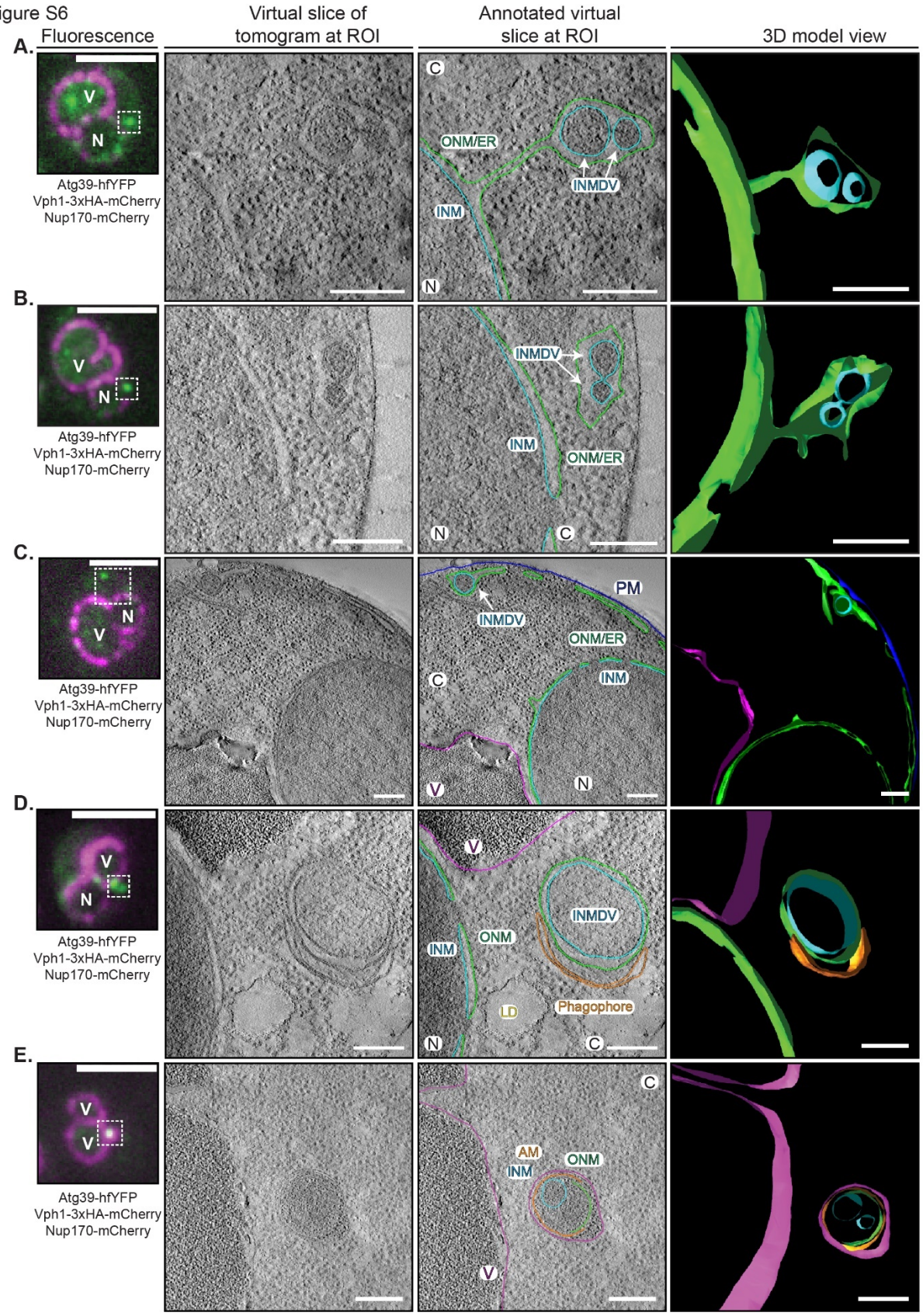

826

Supplemental Figure 6 – Ultrastructure of sites of Atg39 accumulation during nucleophagy.

A-E) CLEM/tomography of sites of Atg39-hfYFP foci. From left to right: fluorescence image of WT cells expressing Atg39-hfYFP (green), Vph1-mCherry and Nup170-mCherry (magenta). Scale bar is 3 µm. EM tomogram acquired of boxed region in fluorescence image and tomogram virtual slice without and with annotation shown alongside a snapshot of a 3D model. Arrows point to INMDVs. ONM is green, INM is light blue, phagophore/autophagosome is orange, vacuole membrane is magenta. Scale bar is 200 nm. C, cytosol; N, nucleus; V, vacuole; ONM, outer nuclear membrane; INM, inner nuclear membrane; ER, endoplasmic reticulum; INMDV, inner nuclear membrane derived vesicle; AM, autophagic membrane. Numbers at right refer to classification scheme in 4F.

827

Figure S7

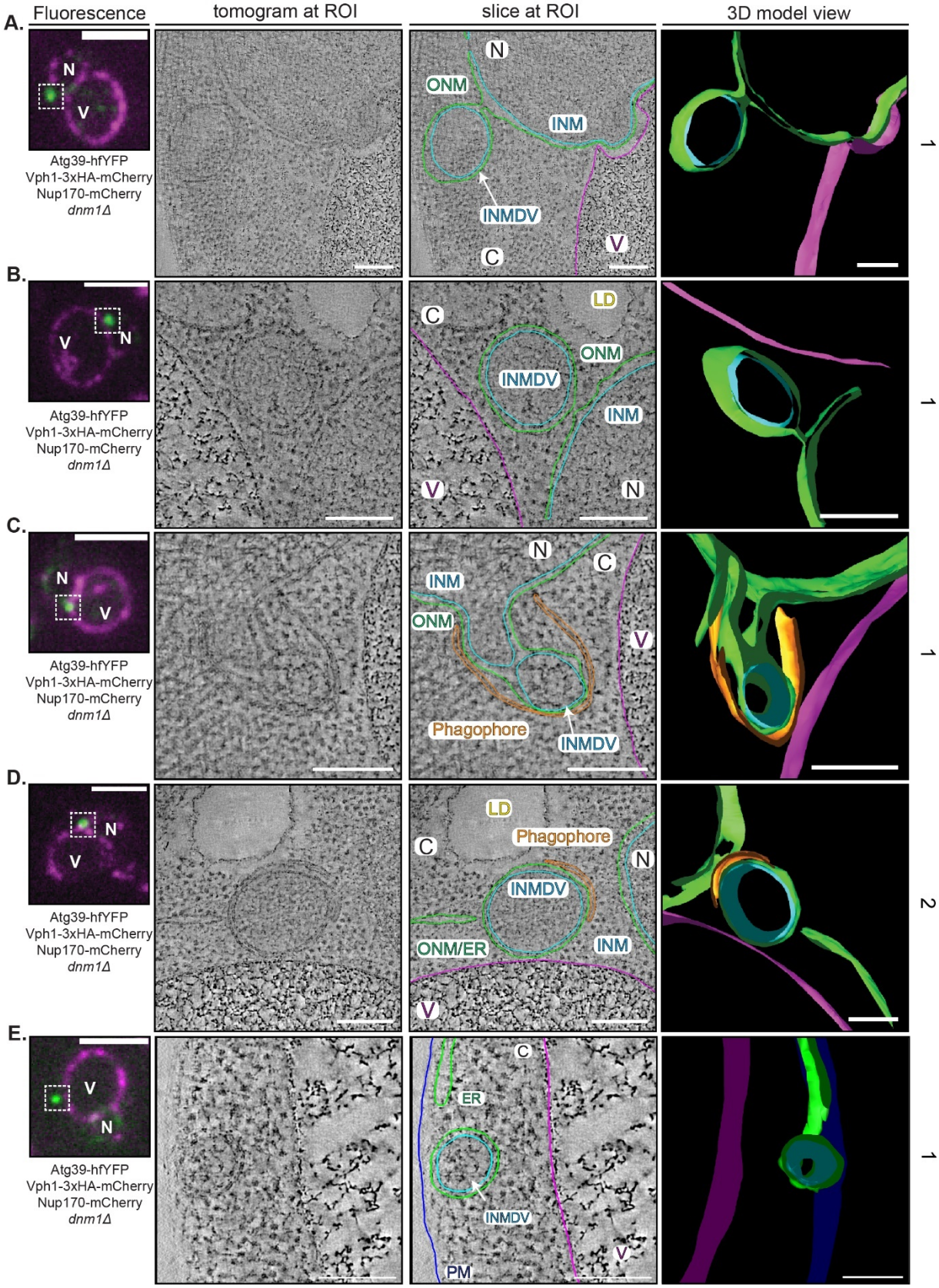

828

Supplemental Figure 7 – Ultrastructure of sites of Atg39 accumulation in *dnm1Δ* cells.

A-E) CLEM/tomography of sites of Atg39-hfYFP foci in *dnm1Δ* cells. From left to right: fluorescence image of WT cells expressing Atg39-hfYFP (green), Vph1-mCherry and Nup170-mCherry (magenta). Scale bar is 3 µm. EM tomogram acquired of boxed region in fluorescence image and tomogram virtual slice without and with annotation shown alongside a snapshot of a 3D model. Arrows point to INMDVs. ONM is green, INM is light blue, phagophore/autophagosome is orange, vacuole membrane is magenta. Scale bar is 200 nm. C, cytosol; N, nucleus; V, vacuole; ONM, outer nuclear membrane; INM, inner nuclear membrane; ER, endoplasmic reticulum; INMDV, inner nuclear membrane derived vesicle; AM, autophagic membrane; LD, lipid droplet. Numbers at right refer to classification scheme in Figure 4F.

829

830

Figure S8

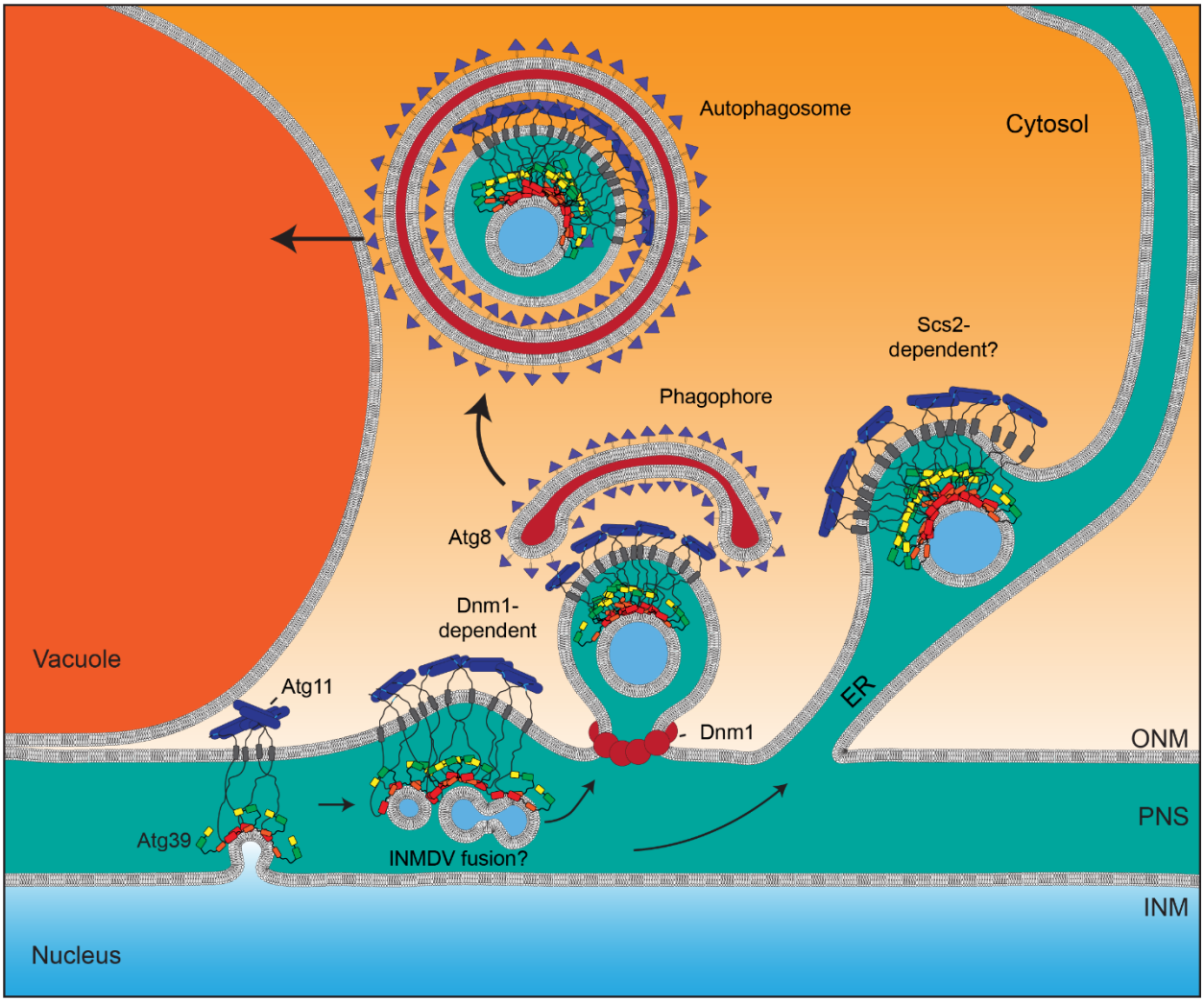

831

Supplemental Figure 8 – Proposed model of nucleophagy.

A) Illustrative model of the molecular and morphological steps of nucleophagy. Atg39 locally accumulates adjacent to the NVJ in a mechanism supported by Atg11 (blue cylinders). It is likely that this clustering coincides with cargo capture and the evagination and fission of the INM to generate an INMDV. Initial small (50-100nm INMDVs) may grow by fusion to generate larger (200-300 nm) INMDVs that are ultimately released from the NE through a Dnm1-dependent ONM fission step, or from the cortical ER through a proposed Scs2-dependent mechanism. Engagement with the phagophore occurs at or just after ONM fission. Autophagosomes containing double membrane nuclear derived vesicles (NDVs) fuse with vacuoles. Some INMDVs may also be capable of transiting through the broader ER but their fate remains uncertain.

832 ## Movies

833 **Movie 1. LLSM movie of Atg39-GFP dynamics in WT cells.** A 5-minute timeseries of cells
834 expressing Atg39-GFP and Vph1-mCherry imaged every 10 seconds by LLSM. Vph1-
835 mCherry signal is rendered as a surface (magenta) and Atg39-GFP foci are rendered as
836 balls (green). Scale bar is 10 μm. Frame rate is 24 frames per second.

837 **Movie 2. CLEM and tomography of potential interface between NDV in an**
838 **autophagosome and the vacuole in a WT cell.** Electron tomogram of a cell expressing
839 Atg39-hfYFP, Nup170-mCherry, and Vph1-mCherry obtained at a site of Atg39-hfYFP
840 accumulation shown in Figure 4D. Note that the outer membrane of the autophagosome
841 and the vacuole extend towards each other but do not touch. However, content with
842 similar electron density of the vacuole lumen is observed between the inner and outer
843 membrane of the autophagosome suggesting prior fusion with the vacuole. NE, green;
844 INMDV, blue; autophagic membranes, orange; vacuole, magenta. Scale bar is 100 nm.

845 **Movie 3. CLEM and tomography of an INMDV within the NE/ER lumen engaged with a**
846 **phagophore in a *dnm1Δ* cell.** Electron tomogram of a cell expressing Atg39-hfYFP,
847 Nup170-mCherry, and Vph1-mCherry in a *dnm1Δ* cell obtained at a region of Atg39-
848 hfYFP accumulation shown in Figure 5D. NE, green; INMDV, blue; autophagic
849 membranes, orange; vacuole, magenta. Scale bar is 100 nm.

850 ## Supplementary Tables

851 **Supplementary Table 1: List of yeast strains used in this study**
852 **Supplementary Table 2: List of plasmids used in this study**
853 **Supplementary Table 3: List of primers used in this study**

854 **References**

855 1. Mannino PJ, Lusk CP. Quality control mechanisms that protect nuclear envelope identity
856 and function. *J Cell Biol*. Sep 5 2022;221(9)doi:10.1083/jcb.202205123
857 2. Mucino-Hernandez G, Acevo-Rodriguez PS, Cabrera-Benitez S, Guerrero AO,
858 Merchant-Larios H, Castro-Obregon S. Nucleophagy contributes to genome stability through
859 degradation of type II topoisomerases A and B and nucleolar components. *J Cell Sci*. Jan 1
860 2023;136(1)doi:10.1242/jcs.260563
861 3. Hasper J, Welle K, Swovick K, Hryhorenko J, Ghaemmaghami S, Buchwalter A. Long
862 lifetime and tissue-specific accumulation of lamin A/C in Hutchinson-Gilford progeria syndrome.
863 *J Cell Biol*. Jan 1 2024;223(1)doi:10.1083/jcb.202307049
864 4. Tsai PL, Zhao C, Turner E, Schlieker C. The Lamin B receptor is essential for cholesterol
865 synthesis and perturbed by disease-causing mutations. *Elife*. Jun 23
866 2016;5doi:10.7554/eLife.16011
867 5. Papandreou ME, Tavernarakis N. Nucleophagy: from homeostasis to disease. *Cell*
868 *Death Differ*. Mar 2019;26(4):630-639. doi:10.1038/s41418-018-0266-5
869 6. Natarajan N, Foresti O, Wendrich K, Stein A, Carvalho P. Quality Control of Protein
870 Complex Assembly by a Transmembrane Recognition Factor. *Mol Cell*. Jan 2 2020;77(1):108-
871 119 e9. doi:10.1016/j.molcel.2019.10.003
872 7. Khmelinskii A, Blaszczak E, Pantazopoulou M, et al. Protein quality control at the inner
873 nuclear membrane. *Nature*. Dec 18 2014;516(7531):410-3. doi:10.1038/nature14096
874 8. Smoyer CJ, Smith SE, Gardner JM, McCroskey S, Unruh JR, Jaspersen SL. Distribution
875 of Proteins at the Inner Nuclear Membrane Is Regulated by the Asi1 E3 Ligase in
876 Saccharomyces cerevisiae. *Genetics*. Apr 2019;211(4):1269-1282.
877 doi:10.1534/genetics.119.301911
878 9. Dou Z, Xu C, Donahue G, et al. Autophagy mediates degradation of nuclear lamina.
879 *Nature*. Nov 5 2015;527(7576):105-9. doi:10.1038/nature15548
880 10. King GA, Goodman JS, Schick JG, et al. Meiotic cellular rejuvenation is coupled to
881 nuclear remodeling in budding yeast. *Elife*. Aug 9 2019;8doi:10.7554/eLife.47156
882 11. King GA, Wettstein R, Varberg JM, et al. Meiotic nuclear pore complex remodeling
883 provides key insights into nuclear basket organization. *J Cell Biol*. Feb 6
884 2023;222(2)doi:10.1083/jcb.202204039
885 12. Mizuno T, Irie K. Msn2/4 transcription factors positively regulate expression of Atg39 ER-
886 phagy receptor. *Sci Rep*. Jun 7 2021;11(1):11919. doi:10.1038/s41598-021-91480-0
887 13. Papandreou ME, Konstantinidis G, Tavernarakis N. Nucleophagy delays aging and
888 preserves germline immortality. *Nat Aging*. Jan 2023;3(1):34-46. doi:10.1038/s43587-022-
889 00327-4
890 14. Wu N, Zheng W, Zhou Y, et al. Autophagy in aging-related diseases and cancer:
891 Principles, regulatory mechanisms and therapeutic potential. *Ageing Research Reviews*.
892 2024;100doi:10.1016/j.arr.2024.102428
893 15. Bahmanyar S, Biggs R, Schuh AL, et al. Spatial control of phospholipid flux restricts
894 endoplasmic reticulum sheet formation to allow nuclear envelope breakdown. *Genes Dev*. Jan
895 15 2014;28(2):121-6. doi:10.1101/gad.230599.113
896 16. Campbell JL, Lorenz A, Witkin KL, Hays T, Loidl J, Cohen-Fix O. Yeast nuclear envelope
897 subdomains with distinct abilities to resist membrane expansion. *Mol Biol Cell*. Apr
898 2006;17(4):1768-78. doi:10.1091/mbc.e05-09-0839
899 17. Romanauska A, Kohler A. Lipid saturation controls nuclear envelope function. *Nat Cell*
900 *Biol*. Sep 2023;25(9):1290-1302. doi:10.1038/s41556-023-01207-8
901 18. Santos-Rosa H, Leung J, Grimsey N, Peak-Chew S, Siniossoglou S. The yeast lipin
902 Smp2 couples phospholipid biosynthesis to nuclear membrane growth. *EMBO J*. 2005;24

19. Barbosa AD, Lim K, Mari M, et al. Compartmentalized Synthesis of Triacylglycerol at the Inner Nuclear Membrane Regulates Nuclear Organization. *Dev Cell*. Sep 23 2019;50(6):755-766 e6. doi:10.1016/j.devcel.2019.07.009
20. Romanauska A, Kohler A. The Inner Nuclear Membrane Is a Metabolically Active Territory that Generates Nuclear Lipid Droplets. *Cell*. Jul 26 2018;174(3):700-715 e18. doi:10.1016/j.cell.2018.05.047
21. Romanauska A, Kohler A. Reprogrammed lipid metabolism protects inner nuclear membrane against unsaturated fat. *Dev Cell*. Sep 27 2021;56(18):2562-2578 e3. doi:10.1016/j.devcel.2021.07.018
22. Melia TJ, Lystad AH, Simonsen A. Autophagosome biogenesis: From membrane growth to closure. *J Cell Biol*. Jun 1 2020;219(6)doi:10.1083/jcb.202002085
23. Eickhorst C, Licheva M, Kraft C. Scaffold proteins in bulk and selective autophagy. *Prog Mol Biol Transl Sci*. 2020;172:15-35. doi:10.1016/bs.pmbts.2020.01.009
24. Kucinska MK, Fedry J, Galli C, et al. TMX4-driven LINC complex disassembly and asymmetric autophagy of the nuclear envelope upon acute ER stress. *Nat Commun*. Jun 13 2023;14(1):3497. doi:10.1038/s41467-023-39172-3
25. Roberts P, Moshitch-Moshkovitz S, Kvam E, O'Toole E, Winey M, Goldfarb DS. Piecemeal microautophagy of nucleus in Saccharomyces cerevisiae. *Mol Biol Cell*. Jan 2003;14(1):129-41. doi:10.1091/mbc.e02-08-0483
26. Allegretti M, Zimmerli CE, Rantos V, et al. In-cell architecture of the nuclear pore and snapshots of its turnover. *Nature*. Oct 2020;586(7831):796-800. doi:10.1038/s41586-020-2670-5
27. Lee CW, Wilfling F, Ronchi P, et al. Selective autophagy degrades nuclear pore complexes. *Nat Cell Biol*. Feb 2020;22(2):159-166. doi:10.1038/s41556-019-0459-2
28. Tomioka Y, Kotani T, Kirisako H, et al. TORC1 inactivation stimulates autophagy of nucleoporin and nuclear pore complexes. *J Cell Biol*. Jul 6 2020;219(7)doi:10.1083/jcb.201910063
29. Mochida K, Oikawa Y, Kimura Y, et al. Receptor-mediated selective autophagy degrades the endoplasmic reticulum and the nucleus. *Nature*. Jun 18 2015;522(7556):359-62. doi:10.1038/nature14506
30. Mizuno T, Muroi K, Irie K. Snf1 AMPK positively regulates ER-phagy via expression control of Atg39 autophagy receptor in yeast ER stress response. *PLoS Genet*. Sep 2020;16(9):e1009053. doi:10.1371/journal.pgen.1009053
31. Otto FB, Thumm M. Mechanistic dissection of macro- and micronucleophagy. *Autophagy*. Mar 2021;17(3):626-639. doi:10.1080/15548627.2020.1725402
32. Chandra S, Mannino PJ, Thaller DJ, et al. Atg39 selectively captures inner nuclear membrane into lumenal vesicles for delivery to the autophagosome. *J Cell Biol*. Dec 6 2021;220(12)doi:10.1083/jcb.202103030
33. Mochida K, Otani T, Katsumata Y, et al. Atg39 links and deforms the outer and inner nuclear membranes in selective autophagy of the nucleus. *J Cell Biol*. Feb 7 2022;221(2)doi:10.1083/jcb.202103178
34. Otsuga D, Keegan BR, Brisch E, et al. The Dynamin-related GTPase, Dnm1p, Controls Mitochondrial Morphology in Yeast. *J Cell Biol*. 1998;143(2)
35. Kuravi K, Nagotu S, Krikken AM, et al. Dynamin-related proteins Vps1p and Dnm1p control peroxisome abundance in Saccharomyces cerevisiae. *J Cell Sci*. Oct 1 2006;119(Pt 19):3994-4001. doi:10.1242/jcs.03166
36. Gonzalez A, Covarrubias-Pinto A, Bhaskara RM, et al. Ubiquitination regulates ER-phagy and remodelling of endoplasmic reticulum. *Nature*. Jun 2023;618(7964):394-401. doi:10.1038/s41586-023-06089-2

952 37. Rosado CJ, Mijaljica D, Hatzinisiriou I, Prescott M, Devenish RJ. Rosella: a fluorescent
953 pH-biosensor for reporting vacuolar turnover of cytosol and organelles in yeast. *Autophagy*. Feb
954 2008;4(2):205-13. doi:10.4161/auto.5331
955 38. Kim J, Kamada Y, Stromhaug PE, et al. Cvt9/Gsa9 Functions in Sequestering Selective
956 Cytosolic Cargo Destined for the Vacuole. *Journal of Cell Biology*. 2001;153(1)
957 39. Kirisako T, Baba M, Ishihara N, et al. Formation Process of Autophogosome is Traced
958 with Apg8/Aut7p in Yeast. *Journal of Cell Biology*. 1999;147(2)
959 40. Kvam E, Goldfarb DS. Nvj1p is the outer-nuclear-membrane receptor for oxysterol-
960 binding protein homolog Osh1p in Saccharomyces cerevisiae. *J Cell Sci*. Oct 1 2004;117(Pt
961 21):4959-68. doi:10.1242/jcs.01372
962 41. Borah S, Thaller DJ, Hakhverdyan Z, et al. Heh2/Man1 may be an evolutionarily
963 conserved sensor of NPC assembly state. *Mol Biol Cell*. Jul 15 2021;32(15):1359-1373.
964 doi:10.1091/mbc.E20-09-0584
965 42. Thaller DJ, Allegretti M, Borah S, Ronchi P, Beck M, Lusk CP. An ESCRT-LEM protein
966 surveillance system is poised to directly monitor the nuclear envelope and nuclear transport
967 system. *Elife*. Apr 3 2019;8doi:10.7554/eLife.45284
968 43. Webster BM, Colombi P, Jager J, Lusk CP. Surveillance of nuclear pore complex
969 assembly by ESCRT-III/Vps4. *Cell*. Oct 9 2014;159(2):388-401. doi:10.1016/j.cell.2014.09.012
970 44. Webster BM, Thaller DJ, Jager J, Ochmann SE, Borah S, Lusk CP. Chm7 and Heh1
971 collaborate to link nuclear pore complex quality control with nuclear envelope sealing. *EMBO J*.
972 2016;35
973 45. Chen S, Cui Y, Parashar S, Novick PJ, Ferro-Novick S. ER-phagy requires Lnp1, a
974 protein that stabilizes rearrangements of the ER network. *Proc Natl Acad Sci U S A*. Jul 3
975 2018;115(27):E6237-E6244. doi:10.1073/pnas.1805032115
976 46. Chen S, Mari M, Parashar S, et al. Vps13 is required for the packaging of the ER into
977 autophagosomes during ER-phagy. *Proc Natl Acad Sci U S A*. Aug 4 2020;117(31):18530-
978 18539. doi:10.1073/pnas.2008923117
979 47. Cui Y, Parashar S, Zahoor M, et al. A COPII subunit acts with an autophagy receptor to
980 target endoplasmic reticulum for degradation. *Science*. Jul 5 2019;365(6448):53-60.
981 doi:10.1126/science.aau9263
982 48. Liu D, Mari M, Li X, Reggiori F, Ferro-Novick S, Novick P. ER-phagy requires the
983 assembly of actin at sites of contact between the cortical ER and endocytic pits. *Proc Natl Acad*
984 *Sci U S A*. Feb 8 2022;119(6)doi:10.1073/pnas.2117554119
985 49. Anwar K, Klemm RW, Condon A, et al. The dynamin-like GTPase Sey1p mediates
986 homotypic ER fusion in S. cerevisiae. *J Cell Biol*. Apr 16 2012;197(2):209-17.
987 doi:10.1083/jcb.201111115
988 50. Voeltz GK, Prinz WA, Shibata Y, Rist JM, Rapoport TA. A class of membrane proteins
989 shaping the tubular endoplasmic reticulum. *Cell*. Feb 10 2006;124(3):573-86.
990 doi:10.1016/j.cell.2005.11.047
991 51. Mozdy AD, McCaffery JM, Shaw JM. Dnm1p GTPase-mediated Mitochondrial Fission Is
992 a Multi-step Process Requiring the Novel Integral Membrane Component Fis1p. *J Cell Biol*.
993 2000;151
994 52. Sesaki H, Southard SM, Yaffe MP, Jensen RE. Mgm1p, a dynamin-related GTPase, is
995 essential for fusion of the mitochondrial outer membrane. *Mol Biol Cell*. Jun 2003;14(6):2342-
996 56. doi:10.1091/mbc.e02-12-0788
997 53. Smaczynska-de R, II, Allwood EG, Aghamohammadzadeh S, Hettema EH, Goldberg
998 MW, Ayscough KR. A role for the dynamin-like protein Vps1 during endocytosis in yeast. *J Cell*
999 *Sci*. Oct 15 2010;123(Pt 20):3496-506. doi:10.1242/jcs.070508
1000 54. Ferguson SM, De Camilli P. Dynamin, a membrane-remodelling GTPase. *Nat Rev Mol*
1001 *Cell Biol*. Jan 11 2012;13(2):75-88. doi:10.1038/nrm3266

1002 55. Mao K, Liu X, Feng Y, Klionsky DJ. The progression of peroxisomal degradation through
1003 autophagy requires peroxisomal division. *Autophagy*. Apr 2014;10(4):652-61.
1004 doi:10.4161/auto.27852
1005 56. Motley AM, Ward GP, Hettema EH. Dnm1p-dependent peroxisome fission requires
1006 Caf4p, Mdv1p and Fis1p. *J Cell Sci*. May 15 2008;121(Pt 10):1633-40. doi:10.1242/jcs.026344
1007 57. Naylor K, Ingerman E, Okreglak V, Marino M, Hinshaw JE, Nunnari J. Mdv1 Interacts
1008 with Assembled Dnm1 to Promote Mitochondrial Division. *Journal of Biological Chemistry*.
1009 2006;281(4):2177-2183. doi:10.1074/jbc.M507943200
1010 58. Mao K, Wang K, Liu X, Klionsky DJ. The scaffold protein Atg11 recruits fission machinery
1011 to drive selective mitochondria degradation by autophagy. *Dev Cell*. Jul 15 2013;26(1):9-18.
1012 doi:10.1016/j.devcel.2013.05.024
1013 59. Hu C, Chinenov Y, Kerppola TK. Visualization of Interactions among bZIP and Rel
1014 Family Proteins in Living Cells Using Bimolecular Fluorescence Complementation. *Molecular*
1015 *Cell*. 2002;9
1016 60. Ader NR, Chen L, Surovtsev IV, et al. An ESCRT grommet cooperates with a diffusion
1017 barrier to maintain nuclear integrity. *Nat Cell Biol*. Oct 2023;25(10):1465-1477.
1018 doi:10.1038/s41556-023-01235-4
1019 61. Bailey MLP, Surovtsev I, Williams JF, et al. Loops and the activity of loop extrusion
1020 factors constrain chromatin dynamics. *Mol Biol Cell*. Jul 1 2023;34(8):ar78.
1021 doi:10.1091/mbc.E23-04-0119
1022 62. Crocker JC, Grier DG. Methods of digital video microscopy for colloidal studies. *Journal*
1023 *of colloid and interface science*. 1996;179
1024 63. Lawrimore J, Bloom KS, Salmon ED. Point centromeres contain more than a single
1025 centromere-specific Cse4 (CENP-A) nucleosome. *J Cell Biol*. Nov 14 2011;195(4):573-82.
1026 doi:10.1083/jcb.201106036
1027 64. Campbell BC, Paez-Segala MG, Looger LL, Petsko GA, Liu CF. Chemically stable
1028 fluorescent proteins for advanced microscopy. *Nat Methods*. Dec 2022;19(12):1612-1621.
1029 doi:10.1038/s41592-022-01660-7
1030 65. Friedman JR, Lackner LL, West M, R. DJ, Nunnari J, Voeltz GK. ER Tubules Mark Sites
1031 of Mitochondrial Division. *Science*. 2011;334
1032 66. Villinger C, Neusser G, Kranz C, Walther P, Mertens T. 3D Analysis of HCMV Induced-
1033 Nuclear Membrane Structures by FIB/SEM Tomography: Insight into an Unprecedented
1034 Membrane Morphology. *Viruses*. Nov 4 2015;7(11):5686-704. doi:10.3390/v7112900
1035 67. Speese SD, Ashley J, Jokhi V, et al. Nuclear envelope budding enables large
1036 ribonucleoprotein particle export during synaptic Wnt signaling. *Cell*. May 11 2012;149(4):832-
1037 46. doi:10.1016/j.cell.2012.03.032
1038 68. Fujioka Y, Tsuji T, Kotani T, et al. 2024;doi:10.1101/2024.08.29.610189
1039 69. Schneider BL, Seufert W, Steiner B, Yang QH, Futcher AB. Use of polymerase chain
1040 reaction epitope tagging for protein tagging in Saccharomyces cerevisiae. *Yeast*. Oct
1041 1995;11(13):1265-74. doi:10.1002/yea.320111306
1042 70. Longtine MS, McKenzie Iii A, Demarini DJ, et al. Additional modules for versatile and
1043 economical PCR-based gene deletion and modification in Saccharomyces cerevisiae. *Yeast*.
1044 1998;14(10):953-961. doi:10.1002/(sici)1097-0061(199807)14:10<953::Aid-yea293>3.0.Co;2-u
1045 71. Zhang Y, Serratore ND, Briggs SD. N-ICE plasmids for generating N-terminal 3 x FLAG
1046 tagged genes that allow inducible, constitutive or endogenous expression in Saccharomyces
1047 cerevisiae. *Yeast*. May 2017;34(5):223-235. doi:10.1002/yea.3226
1048 72. Baudin A, Ozier-Kalogeropoulos OD, A., Lacroute F, Cullin C. A simple and efficient
1049 method for direct gene deletion in *Saccharomyces cerevisiae*. *Nucleic Acids Research*. 1993;21
1050 73. Guldener U, Heck S, Fiedler T, Beinhauer J, Hegemann JH. A new efficient gene
1051 disruption cassette for repeated use in budding yeast. *Nucleic Acids Research*. 1996;24(13)

74. Lacy MM, Baddeley D, Berro J. Single-molecule imaging of the BAR-domain protein Pil1p reveals filament-end dynamics. *Mol Biol Cell*. Aug 15 2017;28(17):2251-2259. doi:10.1091/mbc.E17-04-0238

75. Smoyer CJ, Katta SS, Gardner JM, et al. Analysis of membrane proteins localizing to the inner nuclear envelope in living cells. *J Cell Biol*. Nov 21 2016;215(4):575-590. doi:10.1083/jcb.201607043

76. Chen BC, Legant WR, Wang K, et al. Lattice light-sheet microscopy: imaging molecules to embryos at high spatiotemporal resolution. *Science*. Oct 24 2014;346(6208):1257998. doi:10.1126/science.1257998

77. Adell MAY, Migliano SM, Upadhyayula S, et al. Recruitment dynamics of ESCRT-III and Vps4 to endosomes and implications for reverse membrane budding. *Elife*. Oct 11 2017;6doi:10.7554/eLife.31652

78. Kukulski W, Schorb M, Welsch S, Picco A, Kaksonen M, Briggs JA. Precise, correlated fluorescence microscopy and electron tomography of lowicryl sections using fluorescent fiducial markers. *Methods Cell Biol*. 2012;111:235-57. doi:10.1016/B978-0-12-416026-2.00013-3

79. Mastronarde DN. Automated electron microscope tomography using robust prediction of specimen movements. *J Struct Biol*. Oct 2005;152(1):36-51. doi:10.1016/j.jsb.2005.07.007

80. Kremer JRM, D. N.

McIntosh J. R. Computer Visualization of Three-Dimensional Image Data Using IMOD. *Journal of Structural Biology*. 1996;116(1)

81. Mastronarde DN, Held SR. Automated tilt series alignment and tomographic reconstruction in IMOD. *J Struct Biol*. Feb 2017;197(2):102-113. doi:10.1016/j.jsb.2016.07.011

82. Flajolet P, Gardy D, Thimonier L. Birthday paradox, coupon collectors, caching algorithms and self-organizing search. *Discrete Applied Mathematics*. 1992;39:207-229.

83. Schindelin J, Arganda-Carreras I, Frise E, et al. Fiji: an open-source platform for biological-image analysis. *Nat Methods*. Jun 28 2012;9(7):676-82. doi:10.1038/nmeth.2019

84. Bolte S, Cordelieres FP. A guided tour into subcellular colocalization analysis in light microscopy. *Journal of Microscopy*. 2006;224doi:10.1111/j.1365-2818.2006.01706.x

Supplementary Table 1:Yeast strains used in this study			
Name	***Genotype***	***Origin***	***Generation***
W303a	*MATa, ade2-1 can1-100 his3-11,15 leu2-3,112 trp1-1 ura3-1*	EUROSCARF	
W303α	*MATα, ade2-1 can1-100 his3-11,15 leu2-3,112 trp1-1 ura3-1*	EUROSCARF	
	FIGURE 1		
PMCPL1045	W303, *Atg39-pHluorin-mCherry*	This study	Transformation of PCR product into W303A
PMCPL1078	W303, *Atg39-pHluorin-mCherry atg8Δ::natMX6*	This study	Progeny from cross between PMCPL1045 and PMCPL472
PMCPL1079	W303, *ATG39-pHluorin-mCherry atg11Δ::hphMX6*	This study	Progeny from cross between PMCPL1045 and PMCPL472
PMCPL1253	W303, *ATG39-pHluorin-mCherry nvj1Δ::hphMX6*	This study	Progeny from cross between PMCPL1067 and BWCPL1088
PMCPL1130	W303, *ATG39-pHluorin-mCherry vps13Δ::kanMX6*	This study	Progeny from cross between PMCPL1069 and DTCPL1702
PMCPL1282	W303, *ATG39-pHluorin-mCherry lst1Δ::kanMX6*	This study	Progeny from cross between PMCPL1078 and PMCPL1260
PMCPL1066	W303, *ATG39-pHluorin-mCherry scs2Δ::kanMX6*	This study	Transformation of PCR product into PMCPL1045
PMCPL1249	W303, *ATG39-pHluorin-mCherry lnp1Δ::hphMX6*	This study	Progeny from cross between PMCPL1078 and DTCPL1448
PMCPL1276	W303, *ATG39-pHluorin-mCherry sey1Δ::kanMX6*	This study	Progeny from cross between PMCPL1256 and PMCPL300
PMCPL1243	W303, *ATG39-pHluorin-mCherry rtn1Δ::his3MX6 rtn2Δ::TRP1 yop1Δ::hphMX6*	This study	Progeny from cross between PMCPL1066 and BWCPL176
PMCPL1252	W303, *ATG39-pHluorin-mCherry vps1Δ::his3MX6*	This study	Progeny from cross between PMCPL1067 and PMCPL1094
PMCPL1264	W303, *ATG39-pHluorin-mCherry mgm1Δ::hphMX6*	This study	Progeny from cross between PMCPL1045 and PMCPL1251
PMCPL1067	W303, *ATG39-pHluorin-mCherry dnm1Δ::kanMX6*	This study	Progeny from cross between PMCPL1045 and PMCPL928
PMCPL1127	W303, *ATG39-pHluorin-mCherry heh1Δ::hphMX6*	This study	Progeny from cross between PMCPL1067 and BWCPL1476
PMCPL1293	W303, *ATG39-pHluorin-mCherry heh2Δ::kanMX6*	This study	Progeny from cross between PMCPL1124 and CPL1222
PMCPL1124	W303, *ATG39-pHluorin-mCherry chm7Δ::hphMX6*	This study	Progeny from cross between PMCPL1067 and BWCPL1632
PMCPL1421	W303, *ATG39-pHluorin-mCherry tal1 Δ::kanMX6*	This study	Transformation of PCR product into PMCPL1071
PMCPL1496	W303, *ATG39-pHluorin-mCherry dnm1Δ::kanMX6 vps1Δ::his3MX6*	This study	Progeny of cross between PMCPL1067 and PMCPL1094
PMCPL1430	W303, *ATG39-pHluorin-mCherry heh1Δ::hphMX6 dnm1Δ::kanMX6*	This study	Progeny of cross between PMCPL1127 and PMCPL917
PMCPL1443	W303, *ATG39-pHluorin-mCherry scs2Δ::natMX6 dnm1Δ::kanMX6*	This study	Progeny of cross between PMCPL1430 and PMCPL1422
PMCPL1493	W303, *ATG39-pHluorin-mCherry scs2Δ::natMX6 heh1Δ::hphMX6*	This study	Progeny of cross between PMCPL1127 and PMCPL1422
	FIGURE 2		
PMCPL831	W303, *ATG39-mEGFP DNM1-mCherry::natMX6 pRS406 ATG8pr*	This study	Transformation of linearized plasmid into PMCPL600
PMCPL832	W303, *ATG39-mEGFP DNM1-mCherry::natMX6 pRS406-ATG8pr-DNM1*	This study	Transformation of linearized plasmid into PMCPL600
PMCPL840	W303, *ATG39-mEGFP DNM1-mCherry::natMX6 pRS406-ATG8pr-dnm1(K41A)*	This study	Transformation of linearized plasmid into PMCPL600
PMCPL1320	W303, *ATG39-mEGFP DNM1-mCherry::natMX6 pRS406-ATG8pr fis1Δ::hphMX6*	This study	Transformation of PCR product into PMCPL831
PMCPL1319	W303, *ATG39-mEGFP DNM1-mCherry::natMX6 pRS406 ATG8pr-DNM1 fis1Δ::hphMX6*	This study	Transformation of PCR product into PMCPL840
PMCPL1087	W303, *ATG39-mEGFP DNM1-mCherry::natMX6 pRS406 ATG8pr-dnm1(K41A) fis1Δ::hphMX6*	This study	Transformation of PCR product into PMCPL832
	FIGURE 3		
PMCPL940	W303, *ATG39-mEGFP VPH1-3xHA-mCherry::natMX6*	This study	Progeny from cross between PMCPL856 and PMCPL922
PMCPL857	W303, *ATG39-mEGFP VPH1-3xHA-mCherry::natMX6 NUP170-mCherry::kanMX6 dnm1Δ::TRP1*	This study	Progeny from cross between PMCPL851 and PMCPL608
MKSP3186	*fta3::fta3-mEGFP::kanMX6 leu1-32 ura3-D18 ade6-M210*	Ader et al., 2023	
	FIGURE 4		
PMCPL1283	W303, *ATG39-hfYFP VPH1-3xHA-mCherry::natMX6 NUP170-mCherry::kanMX6*	This study	Progeny from cross between PMCPL1257 and PMCPL850
PMCPL1390	W303, *ATG39-hfYFP VPH1-3xHA-mCherry::natMX6 NUP170-mCherry::kanMX6 dnm1Δ::TRP1*	This study	Progeny from cross between PMCPL1283 and PMCPL785
	FIGURE 5		
PMCPL1390	W303, *ATG39-hfYFP VPH1-3xHA-mCherry::natMX6 NUP170-mCherry::kanMX6 dnm1Δ::TRP1*	This study	Progeny from cross between PMCPL1283 and PMCPL785
	FIGURE S1		
PMCPL1263	W303, *ATG39-3xHA::his3MX6*	This study	Progeny from cross between PMCPL300 and SCCPL117
PMCPL578	W303, *ATG39-3xHA*	This study	Transformation of PCR product into W303A
PMCPL521	W303, *ATG39-mEGFP::kanMX6*	This study	Transformation of PCR product into W303A
PMCPL1193	W303, *ATG39-mEGFP*	This study	Transformation of PCR product into W303A
W303a	*MATa, ade2-1 can1-100 his3-11,15 leu2-3,112 trp1-1 ura3-1*	EUROSCARF	
PMCPL1071	W303, *Atg39-pHluorin-mCherry*	This study	Progeny from cross between PMCPL1045 and PMCPL898
PMCPL1080	W303, *Atg39-pHluorin-mCherry atg8Δ::natMX6 atg11Δ::hphMX6*	This study	Progeny from cross between PMCPL1045 and PMCPL472
PMCPL1079	W303, *ATG39-pHluorin-mCherry atg11Δ::hphMX6*	This study	Progeny from cross between PMCPL1045 and PMCPL472
PMCPL1066	W303, *ATG39-pHluorin-mCherry scs2Δ::kanMX6*	This study	Transformation of PMCPL1045 with PCR product
PMCPL1067	W303, *ATG39-pHluorin-mCherry dnm1Δ::kanMX6*	This study	Progeny from cross between PMCPL1045 and PMCPL928
PMCPL1443	W303, *ATG39-pHluorin-mCherry scs2Δ::natMX6 dnm1Δ::kanMX6*	This study	Progeny of cross between PMCPL1430 and PMCPL1422
PMCPL1127	W303, *ATG39-pHluorin-mCherry heh1Δ::hphMX6*	This study	Progeny from cross between PMCPL1067 and BWCPL1476
	FIGURE S2		
PMCPL1320	W303, *ATG39-mEGFP DNM1-mCherry::natMX6 pRS406-ATG8pr fis1Δ::hphMX6*	This study	Transformation of PCR product into PMCPL831
PMCPL1319	W303, *ATG39-mEGFP DNM1-mCherry::natMX6 pRS406 ATG8pr-DNM1 fis1Δ::hphMX6*	This study	Transformation of PCR product into PMCPL840
PMCPL1087	W303, *ATG39-mEGFP DNM1-mCherry::natMX6 pRS406 ATG8pr-dnm1(K41A) fis1Δ::hphMX6*	This study	Transformation of PCR product into PMCPL832
	FIGURE S3		
PMCPL1584	W303, *ATG39-phluorin DNM1-mCherry::natMX6 pRS406-ATG8pr* fis1Δ::kanMX6	This study	Transformation of PCR product into PMCPL1577
PMCPL1571	W303, *ATG39-phluorin DNM1-mCherry::natMX6 pRS406-ATG8pr fis1Δ::kanMX6 atg11Δ::hphMX6*	This study	Transformation of PCR product into PMCPL1568
PMCPL1186	W303, *ATG39-phluorin DNM1-mCherry::natMX6 pRS406-ATG8pr-DNM1 fis1Δ::kanMX6*	This study	Transformation of PCR product into PMCPL1108
PMCPL1114	W303, *ATG39-phluorin DNM1-mCherry::natMX6 pRS406-ATG8pr-DNM1 fis1Δ::kanMX6 atg11Δ::hphMX6*	This study	Transformation of PCR product into PMCPL1109
PMCPL1112	W303, *ATG39-phluorin DNM1-mCherry::natMX6 pRS406-dnm1(K41A) fis1Δ::hphMX6*	This study	Transformation of PCR product into PMCPL1110
PMCPL1113	W303, *ATG39-phluorin DNM1-mCherry::natMX6 pRS406-dnm1(K41A) fis1Δ::kanMX6 atg11Δ::hphMX6*	This study	Transformation of PCR product into PMCPL1111
PMCPL1010	W303, *ATG39-ymTurquoise2 VC-ATG11 DNM1-VN::kanMX6*	This study	Progeny of cross between PMCPL998 and PMCPL1001
PMCPL1585	W303, *ATG39-ymTurquoise2 VC-ATG11 dnm1-1-727-VN::his3MX6*	This study	Progeny of cross between PMCPL1569 and PMCPL1010
	FIGURE S4		
PMCPL1450	W303, ATG39-mEGFP 2x-mCherry-ATG8::hphMX6	This study	Progeny of cross between PMCPL577 and MG01
PMCPL1134	W303, *ATG39-mEGFP VPH1-3xHA-mCherry::natMX6 NUP170-mCherry::kanMX6 atg11Δ::hphMX6*	This study	Progeny of cross between PMCPL857 BWCPL1376
PMCPL940	W303, *ATG39-mEGFP VPH1-3xHA-mCherry::natMX6*	This study	Progeny from cross between PMCPL856 and PMCPL922
PMCPL857	W303, *ATG39-mEGFP VPH1-3xHA-mCherry::natMX6 NUP170-mCherry::kanMX6 dnm1Δ::TRP1*	This study	Progeny from cross between PMCPL851 and PMCPL608
PMCPL940	W303, *ATG39-mEGFP VPH1-3xHA-mCherry::natMX6*	This study	Progeny from cross between PMCPL856 and PMCPL922
	FIGURE S5		
PMCPL940	W303, *ATG39-mEGFP VPH1-3xHA-mCherry::natMX6*	This study	Progeny from cross between PMCPL856 and PMCPL922
PMCPL857	W303, *ATG39-mEGFP VPH1-3xHA-mCherry::natMX6 NUP170-mCherry::kanMX6 dnm1Δ::TRP1*	This study	Progeny from cross between PMCPL851 and PMCPL608
PMCPL1132	W303, *ATG39-mEGFP pRS405-heh1-1-476-2xmCherry*	This study	Transformation of linearized plasmid into PMCPL1120
	FIGURE S6		
PMCPL1283	W303, *ATG39-hfYFP VPH1-3xHA-mCherry::natMX6 NUP170-mCherry::kanMX6*	This study	Progeny from cross between PMCPL1257 and PMCPL850
	FIGURE S7		
PMCPL1390	W303, *ATG39-hfYFP VPH1-3xHA-mCherry::natMX6 NUP170-mCherry::kanMX6 dnm1Δ::TRP1*	This study	Progeny from cross between PMCPL1283 and PMCPL785

Supplementary Table 2: Plasmids used in this study

Name	*Description*	*Origin*
pFa6a-mEGFP-kanMX6	Template for PCR based chromosomal integration of mEGFP ORF	Lacy et al. 2017
pFA6a-hphMX6	Template for PCR based chromosomal integration of hphMX6 cassette	Longtine et al. 1998
pFA6a-natMX6	Template for PCR based chromosomal integration of natMX6 cassette	Van Driessche et al. 2005
pFA6a-kanMX6	Template for PCR based chromosomal integration of kanMX6 cassette	Bahler J. et al. 1998
pAS1NB	Template for cloning pPM27	Rosado et al. 2008
pSJ1321	Template for cloning pPM30	Smoyer et al. 2016
pFA6a-3xHA-mCherry-natMX	Template for PCR based chromosomal integration of 3xHA-mCherry ORF	This study
pFA6a-3xHA-his3MX6	Template for PCR based chromosomal integration of 3xHA	Longtine et al. 1998
pPM09	mEGFP-loxP-kanMX6-loxP	This study
pPM26	3xHA-loxP-kanMX6-loxP	This study
pPM31	hfYFP-loxP-kanMX6-loxP	This study
pPM27	pHlourin-loxP-kanMX6-loxP	This study
pPM28	pHlourin-mCherry-loxP-kanMX6-loxP	This study
pFA6a-mCherry-kanMX6	Template for PCR based chromosomal integration of mCherry ORF	This study
pPM03	pRS406 ATG8pr	This study
pPM11	pRS406 ATG8pr-*DNM1*	This study
pPM15	pRS406 *dnm1 (K41A)*	This study
pSH47	pRS416 *GAL1-CRE*	Güldener et al. 1996
pPM29	pRS405 heh1-1-479-mCherry	This study
pPM30	pRS405 heh1-1-479-2xmCherry	This study
pPM32	mCherry-loxP-kanMX6-loxP	This study

Supplementary Table 3: Primers used in this study

Purpose	*Name*	*Sequence*
Atg39 C-terminal tag cassette construction	F2 ATG39	TCGAGGATGTATAAAGCGATGTCAGAATGCAGGAAAAAAAATTATTTTAAGTGCAAACAC-CGGATCCCCGGGTTAATTAA
	R1 ATG39	TAAGCAGTCGTTTTTTTTTTCTTTTGTTAATTTCATTCTTCATGCTGGGTTTTGGATGAT-GAATTCGAGCTCGTTTAAAC
	P1.4 ATG39	TAAGCAGTCGTTTTTTTTTTCTTTTGTTAATTTCATTCTTCATGCTGGGTTTTGGATGAT-atggtgtcgacaacccttaat
	F5 GFP ATG39	TCGAGGATGTATAAAGCGATGTCAGAATGCAGGAAAAAAAATTATTTTAAGTGCAAACAC-AAAGGAGAAGAACTTTTCACTGG
	F5 HA ATG39	TCGAGGATGTATAAAGCGATGTCAGAATGCAGGAAAAAAAATTATTTTAAGTGCAAACAC-gccactagtTACCCATACGAT
	F5 hfYFP ATG39	TCGAGGATGTATAAAGCGATGTCAGAATGCAGGAAAAAAAATTATTTTAAGTGCAAACAC-GTATCCAAGGGTGAGGAATTG
Vph1 C-terminal tag cassette construction	F2 VPH1	GCATTTGAGTATAAAGACATGGAAGTCGCTGTTGCTAGTGCAAGCTCTTCCGCTTCAAGC-CGGATCCCCGGGTTAATTAA
	R1 VPH1	ATGGTCACTGGTGGATTGGATTGCAAGTCTAACGTTTTCATGAGATAAGTTTGGCTTTCC-GAATTCGAGCTCGTTTAAAC
Nup170 C-terminal tag cassette construction	F2 NUP170	CCAATTGAAAAGTACGTTAAGAACAGCGGCAATAATTTGGGGATTTGTTTCTACAAAGAA-CGGATCCCCGGGTTAATTAA
	R1 NUP170	ACCTTTATCTTAAGGAAAAGTTCACTCGATATTCTTAACTTTACCGTCTAGTAAGGCCTC-GAATTCGAGCTCGTTTAAAC
scs2Δ cassette construction	F1 SCS2	CGCACATTCTGTGTTAATAGTGTAGCAGAAGGGTATTCTACAATCTCCGCGAACCTAAGT-CGGATCCCCGGGTTAATTAA
	R1 SCS2	GGAAAGGGCAAAACACACACATATATAAATATATATTTAGAATACAGCTATATCCTCAATCTCCC-GAATTCGAGCTCGTTTAAAC
fis1Δ cassette construction	F1 FIS1	ATACCTTGCGTAAAAACGGCACATAGAAGCACAGATCAGAGCACAGCCATACAACATAAG-CGGATCCCCGGGTTAATTAA
	R1 FIS1	TACGCGTGCGTGCGATTCATTCTTATGTATGTACGTATGTGCTGATTTTTTATGTGCTTG-GAATTCGAGCTCGTTTAAAC
RTqPCR primers	sATG39 qPCR 6	TGAAAGACGGTTGGCACAAG
	asATG39 qPCR	ACCCTTAAACTTTCTTGAGCGG
	sATG8 qPCR	GAAGGCCATCTTCATTTTTGTC
	asATG8 qPCR	TTCTCCTGAGTAAGTGACATAC
	sATG11 qPCR	GCAGACGTAGATCTTTCGCG
	asATG11 qPCR	TGTGAGCAAACGGTTAAGCC
	sATG40 qPCR	GAGACCCTTTGTAACGGAGC
	asATG40 qPCR	CATTCGGGAACTCAGTGCTG
	sACT1 qPCR	TGGATTCCGGTGATGGTGTT
	asACT1 qPCR	TCAAAATGGCGTGAGGTAGAG